Structural Design and Analysis of a 3U CubeSat-based rover for lunar exploration

Author: Panin Ananwatanyoo

Date: August 8, 2025

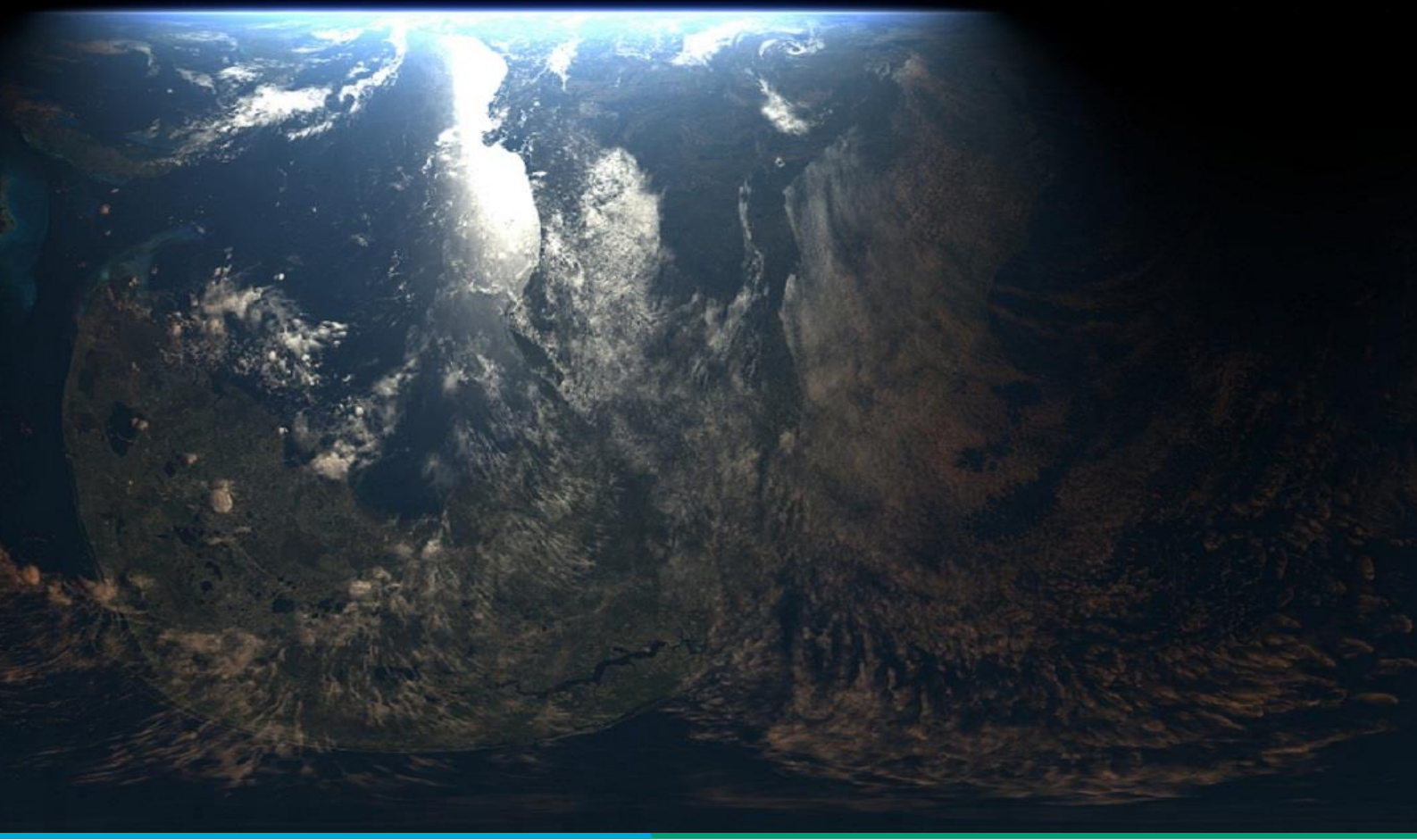

Structural Design, Analysis, and Validation of a 3U CubeSat-based rover for lunar exploration

By

Panin Ananwatanyoo

In partial fulfilment of the requirements for the degree of:

Master of Science
in Aerospace Engineering

at the Delft University of Technology,
to be defended publicly on Thursday August 28, 2025 at 9.30 AM.

Supervisors:	Asst. Prof. Dr. Vahid Y. Nasrabadi,	TU Delft
	Dr. Mojtaba Raouf	Leiden University
	Prof. Bernard Foing	ILEWG LUNEX EuroMoonMars
Thesis committee:	Assoc. Prof. Dr. P. P. Sundaramoorthy,	TU Delft
	Prof. Dr. Nathan Eskue,	TU Delft

Preface

This thesis presents the outcome of my Master of Science research project at Delft University of Technology, Aerospace Engineering, conducted in collaboration with Leiden Observatory and Inholland University of Applied Sciences. The project, which focused on the structural and thermal design of a lunar CubeSat-based rover, represents the culmination of my passion for space exploration and space systems engineering. Over the course of this work, I have had the opportunity to engage with numerous experts in the field of planetary robotics, structural simulation, and thermal control.

I am grateful to my supervisors and thesis committee members for their lessons and feedback throughout this project. The interdisciplinary nature of this research required me to navigate challenges across mechanical design, simulation validation, and experimental mobility testing. I also acknowledge the support of my colleagues and peers. Lastly, I am sincerely grateful to my friends in Delft who always supported me during my time in Delft.

This work is dedicated to advancing the feasibility of small, cost-effective platforms for planetary science. I hope that the findings and methodology presented here will serve as a useful reference for future missions aiming to push the boundaries of CubeSat capabilities.

Contents

Abstract

This thesis presents the structural and thermal design of a CubeSat-based rover system for lunar surface exploration, developed with standard 3U CubeSat as foundation. The study focuses on the integration of a mobility platform, capable of being deployed from a lunar lander, on to the 3U CubeSat. Detailed finite element analysis (FEA) was conducted to ensure structural survivability under launch conditions, including quasi-static, random vibration, and shock loads. The first natural frequency was found to be 267 Hz, exceeding the 115 Hz threshold across major spacecraft launchers. Maximum von Mises stress reached 300 MPa under the worst-case shock loading, yielding a minimum margin of safety of 0.10. Thermal analysis using passive insulation strategies demonstrated that all subsystem components remained within -20°C to +65°C under lunar surface conditions. Mobility performance was validated through terramechanics modelling and field testing on Earth's sandy terrain, where the prototype exhibited static and dynamic sinkage within 11% and 9% of analytical predictions, respectively. These results demonstrate that with appropriate design strategies and material selection, a CubeSat-Based Rover configuration can be feasibly integrated within a 3U CubeSat. While further studies—such as radiation tolerance, dust mitigation, lunar analogue terrain testing, and structural testing—are required, the findings highlight the potential of this architecture as a standardized, low-cost platform for short-duration lunar surface missions.

Acknowledgments

I would like to thank my Leiden University professors, Dr. Mojtaba Raouf and Dr. Bernard Foing, for initiating this project and providing continuous guidance throughout its development. I am also grateful to my thesis supervisor, Dr. Vahid Yaghoubi Nasrabadi, for his valuable feedback on the finite element analysis and thesis planning. Special thanks to my teammates and collaborators in the EMEC1 and EMEC2 missions for their efforts in orbit calculation and subsystem development. Lastly, I acknowledge the support from TU Delft and the associated facilities that enabled the prototyping phases of this work.

1 Introduction

CubeSats have revolutionized access to space through their compact form factor, standardized interfaces, and cost-effective development cycles. Initially conceived as educational tools, they have since evolved into viable platforms for a wide range of scientific, commercial, and exploratory missions. With growing interest in extending CubeSat capabilities beyond Earth orbit, these miniature satellites are now being considered for planetary exploration, including lunar surface operations.

Despite their advantages, adapting CubeSats for surface mobility poses significant engineering challenges. The 3U form factor, while compact and modular, imposes strict limitations on mass, volume, power availability, and structural robustness. Furthermore, lunar missions introduce harsh environmental factors including extreme thermal variation, abrasive regolith, and shock loads during launch, landing, and deployment. For instance, structural loads during lunar landing can exceed random vibration levels of 0.035 g^2/Hz seen when comparing typical CubeSat Launchers like Arianne 6 [1] to the Penegrine lunar lander [2]. The lunar surface temperature can reach up to +127 ℃ during the day which can induce more thermal stress to the structure [3]. Additionally, lunar regolith exhibits low soil cohesion (0.1–1 kPa) and sharp angular soil particles, complicating traction and increasing abrasion risk for mobility mechanisms [4].

To address these issues, the EMEC (Earth-Moon Exploration CubeSat) program was initiated by LUNEX-EuroMoonMars [5], targeting the development of a deployable rover from a standard 3U CubeSat bus. The second phase of this program, EMEC2, focuses on the design and development of a structurally reinforced and thermally stable CubeSat-based rover capable of short-duration lunar surface exploration, using a standard 3U Earth Observation CubeSat design from the first phase of the program, EMEC1, as reference [5]. The EMEC2 system features a compact rover with four independently driven wheels, designed to be deployed from a lunar lander. The rover must operate autonomously after deployment, necessitating the ability to withstand launch and landing loads and to survive the harsh thermal and environmental conditions of the lunar surface.

This thesis presents the complete design and validation process for the EMEC2 CubeSat-based rover, including finite element simulations under quasi-static, vibrational, and shock loads, thermal simulations for both eclipse and sunlit conditions, and field testing of the mobility subsystem on a regolith analogue terrain. The project demonstrates that with careful material selection, subsystem integration, and simulation-driven design, a viable CubeSat-based mobile platform can be achieved, offering a path forward for low-cost lunar surface science missions.

1.1 Research Question

The use of CubeSats for deep-space missions, including planetary surface exploration, is an emerging field that promises to reduce mission cost and development time. However, integrating a mobile robotic system within the limited volume and mass budget of a 3U CubeSat poses considerable design challenges. This project seeks to address the question: **Can a standard 3U CubeSat platform be modified to effectively support the integration, deployment, and operation of a structurally robust, thermally controlled, and mobility-capable lunar surface rover?**

The research question is explored by addressing multiple subdomains: (i) the structural feasibility of deploying a rover from a CubeSat frame under launch and impact conditions, (ii) the effectiveness of a passive thermal control system in lunar conditions, and (iii) the mechanical capability of the 3U CubeSat-scale wheel system to traverse a lunar analogue terrain.

1.2 Scope of Work

This thesis focuses on the design, analysis, and validation of a CubeSat-based rover system under the EMEC2 mission concept. The scope includes:

- Structural design and finite element (FE) modeling of the CubeSat structure and deployable rover, including static, vibrational, and shock load cases.
- Sensitivity analysis of FE model
- Model-based validation of FE model using synthetic data
- Thermal analysis using simplified worst-case lunar conditions to assess the feasibility of passive thermal control.
- Mobility system design, supported by terramechanics modelling which is verified through prototype field testing on Earth's sandy terrain.
- Mock-up Prototype system integration to assess design assembly process.

The study does not include the detailed design of avionics or communication systems and assumes the existence of a suitable lunar lander deployment interface, using Penegrine Lander Payload User Manual as reference [2]. Focus is placed on verifying the rover's structural and thermal survivability as well as mechanical mobility performance.

1.3 High-level System Requirements

The following system-level requirements were defined based on relevant industry standards (e.g., ESA ECSS), mission constraints, expected lunar environmental conditions, and customer requirements, namely Leiden University. These criteria guided the design and validation of the EMEC2 CubeSat-based rover:

- **Form Factor**: The CubeSat frame shall fit within standard 3U CubeSat dimension.
- **Mass Budget**: The mass of the CubeSat component shall remain below 6 kg. The total mass of EMEC2 CubeSat-based rover shall remain below 8 kg.
- **Structural Integrity**: The structure shall not yield under quasi-static loads, random vibrations, and shock loads from potential launch vehicles and lunar lander.
- **Natural Frequency**: The first mode shall exceed 115 Hz to avoid resonance with vehicle dynamics.
- **Thermal Viability**: The system shall maintain all internal components within their operational temperature limits throughout the mission.
- **Mobility Capability**: The rover shall be able to traverse soft lunar-analogue terrain and generate sufficient traction without excessive sinkage or wheel slip.

These requirements serve as the basis for the simulations, design decisions, and validation efforts presented in this work.

2 Literature Review

CubeSat concept was first introduced by Jordi Puig-Suari and Bob Twiggs in 1999 to create a standardized satellite platform for educational and research purposes [6]. The development of CubeSat-compatible commercial off-the-shelf (COTS) components has further reduced the cost of CubeSat systems, enabling missions with imaging sensors, spectrometers, radiation monitors, and propulsion system, at a fraction of traditional cost [7]. JAXA's OMOTENASHI missions, shown in Figure 1, are prominent examples of CubeSats being tested for lunar surface exploration, emphasizing their developing role in lunar space programs [8].

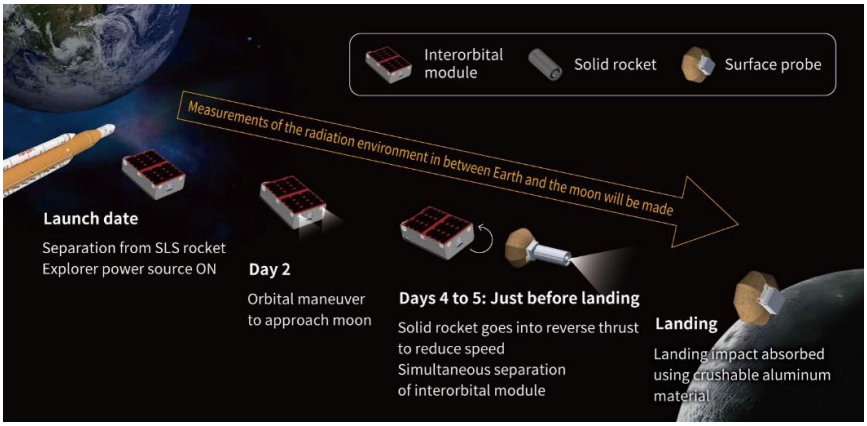

Figure 1: OMOTENASHI mission profile [8]

The CubeSat Design Specification (CDS) provides guidelines for CubeSat structural design, interface requirements, and testing protocols [9]. For this thesis, the CubeSat's dimensions are restricted to a 3U configuration. From CDS, 3U CubeSat dimensions are shown in Figure 2 below.

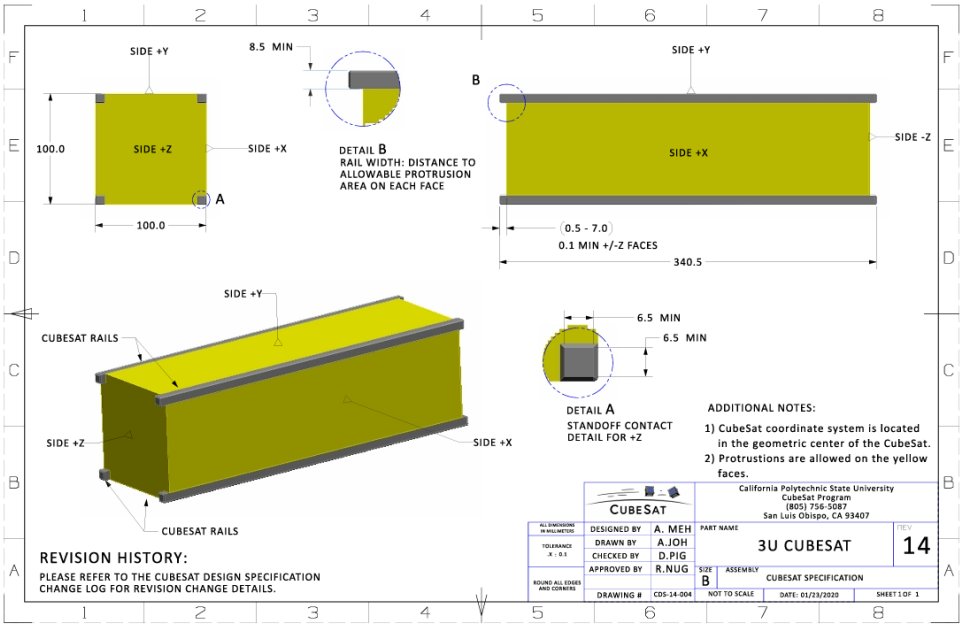

Figure 2: 3U CubeSat Specification Drawing [9]

2.1 CubeSat-Based Rover

However, implementing mobility systems with the 3U CubeSat poses additional structural, thermal, and mechanical challenges. Most past efforts have focused on orbiters or passive landers [8] [10]. More recent concepts, such as the HiveR [11] and CubeRover [12] shown in Figure 3, highlight growing interest in standardized, rover-capable platforms. To reduce rover complexity, CubeSat-based rovers have been developed and offer the prospect for standardization, similar to how CubeSats brought values to the economics of Low-Earth Orbit Satellites. The term “CubeSat-based” refers to the incorporation of CubeSat technology in these rovers, including COTS electronics and CubeSat structures themselves.

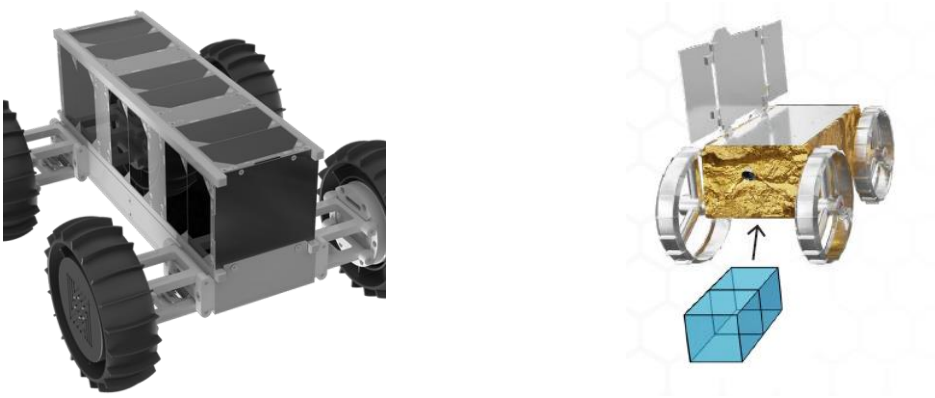

(a) NEUROSPACE HiveR (b) Astrobotics CubeRover

Figure 3: State-of-the-art Lunar CubeSat-based Rover [13]

These initiatives focus on modularity and subsystem component qualification, but lack full-scale validation with standardized CubeSat constraints, especially structure and thermal design. This thesis aims to address full-scale validation on these aspects for lunar surface deployment.

2.2 Spacecraft Radiation Tolerance

Due to limited time, radiation analysis has not been thoroughly investigated and was only briefly explored. ECSS-Q-ST-60-15C (Radiation Hardness Assurance for Electrical, Electronic, and Electromechanical (EEE) components) defines material shielding and radiation tolerance criteria to protect avionics and communication systems from typical radiation exposure. The standard addresses the three main radiation effects on EEE components: Total Ionizing Dose (TID), Displacement Damage or Total Non-Ionizing Dose, and Single event Effects (SEE). [14]

Recent research by Thomsen et al. [15] has explored the effectiveness of CubeSat aluminium alloy wall structures under different radiation exposure scenarios. The study highlights that aluminium provides baseline shielding, but additional materials such as polyethylene or composite layers can significantly enhance protection against high-energy protons. The shielding effectiveness is largely dependent on thickness, with a 4.44 mm aluminium layer showing notable reductions in radiation dosage compared to standard 1 mm CubeSat walls. However, the study also emphasizes the trade-off that must be made between added mass and shielding efficiency.

In this thesis, all selected electronic components are manufactured and tested by EnduroSat, which are space-grade COTS components. The components are tested to tolerate 40,000 rad in silicon TID which is equivalent to 15 years of radiation in Low Earth Orbit (LEO), unshielded [16]. SEE tests are conducted with 1 MeV protons on unshielded electronic boards to ensure devices are not susceptible to soft errors [16]. However, the effect of additional shielding from CubeSat aluminium structure panels has not been investigated.

2.3 Rover Steering Concepts

Steering system selection is one of the most crucial aspects in ensuring the rover's maneuverability and terrain adaptability. Five steering options commonly used in modern rover designs are Ackermann Steering, Skid Steering, Articulated Frame Steering, Crab Steering, and passive steering. A picture of each steering concept is shown in Figure 4. Ackermann steering provides precise control and is well-suited for hard surfaces, while skid steering, widely used in planetary rovers, offers simplicity and effectiveness on loose regolith but suffers from high energy consumption. Articulated frame steering enhances flexibility on uneven terrain by enabling the frame to bend at multiple joints, improving traction and maneuverability. Crab steering allows the wheels to turn in the same direction, enabling diagonal movement. Passive steering adds another layer of spring restoring force to suppress unintended steering or misalignment when transversing uneven terrain. Each steering system presents trade-offs in terms of control complexity, turning radius, energy efficiency, and terrain adaptability, which must be carefully evaluated during the design process. [17]

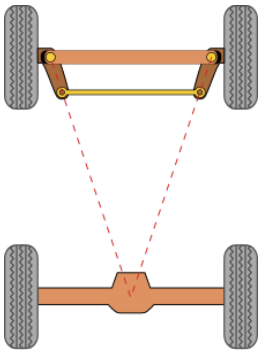

Ackerman Steering

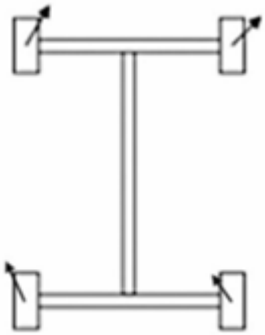

Skid Steering

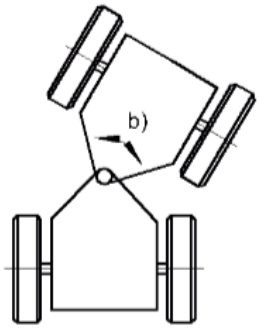

Articulated Frame Steering

Crab Steering

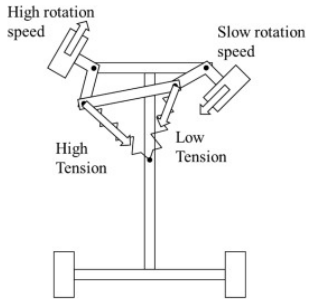

Passive Steering

Figure 4: State-of-the-art steering concepts. [17]

2.4 Rover Wheel Concept

Three rover wheel concepts were discovered through literature review [4]. These concepts are shown in Figure 5.

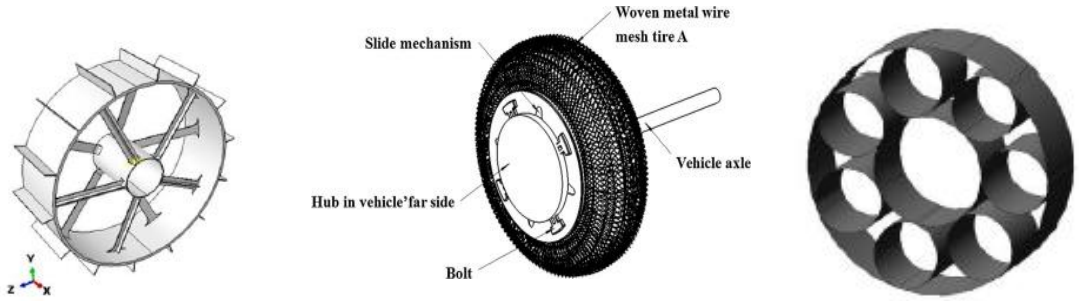

(a) Rigid wheel with grousers (b) Flexible Wire Mesh Wheel (c) Hoop Spring Wheel

Figure 5: Existing Rover Wheel Concepts

Three prominent rover wheel concepts—rigid wheels with grousers, flexible wire mesh wheels, and hoop spring wheels—offer distinct advantages and drawbacks for lunar surface mobility. Rigid wheels are simple to manufacture, but their lack of adaptability and shock absorption makes them less effective on uneven or rocky surfaces. Flexible wire mesh wheels conform well to terrain and absorb shocks efficiently, making them ideal for lunar regolith environments. However, they are complex to fabricate, especially for small size rovers like 3U CubeSat-Based rovers. Hoop spring wheels combine flexibility and shock resistance with an adaptive wheel structure, offering a balanced performance, but require precise design to manage fatigue and load capacity. The optimal choice depends on mission requirements, durability considerations, and their compatibility with 3U CubeSat size rover.

2.5 Wheel Traction and Terramechanics Analysis

For conventional rovers, rover wheel design is critical for ensuring sufficient traction and stability on the reduced-gravity lunar surface. Alhammadi demonstrated the use of terramechanics analysis to perform lunar rover wheel sizing, including the integration of grousers to improve traction in loose lunar regolith [4]. Wheel thrust force and sinkage were derived from wheel-soil interaction force diagram shown in Figure 6. This derivation resulted in the governing equation (4) and (5). later used to determine EMEC2 wheel size as shown in the wheel design Section 3.1.1.

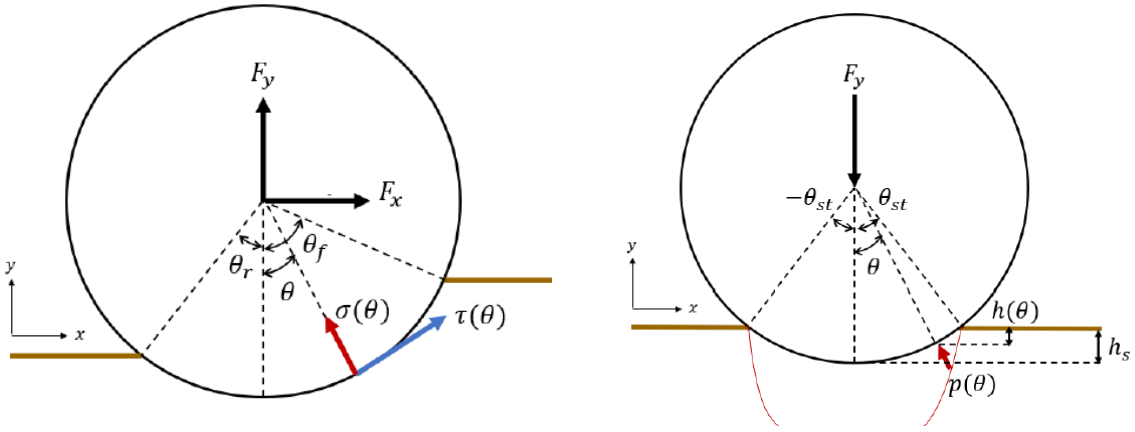

(a) Wheel Stress & Force Diagram (b) Wheel Static Sinkage Geometry

Figure 6: Wheel-soil Interaction Free body diagram [4]

2.6 Existing Rover Deployment Concepts

Three typical rover deployment concepts, for small lunar rovers, were found from literature review. One is the lander ramp deployment concept shown in Figure 7. A ramp is initially folded and attached to the lander. After landing on the moon, the ramp is unfolded and the rover unfixed from the lander. The rover then moves itself out of the lander.

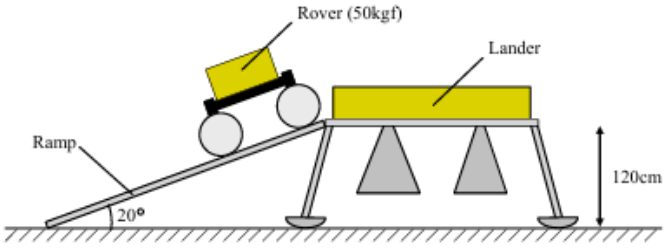

Figure 7: Lander Ramp deployment concept [18]

The second deployment concept found is the tethered rover concept as shown in Figure 8. Rovers are fixed hanging beside landers with tether connects to the rover. The rover is then slowly lowered while being tethered to the lander. After the rover lands on the lunar surface, the tether disconnects, and deployment is finished. It is also possible to utilize a robotic arm instead of a tether to support the rover weight for the lowering of rover onto lunar surface.

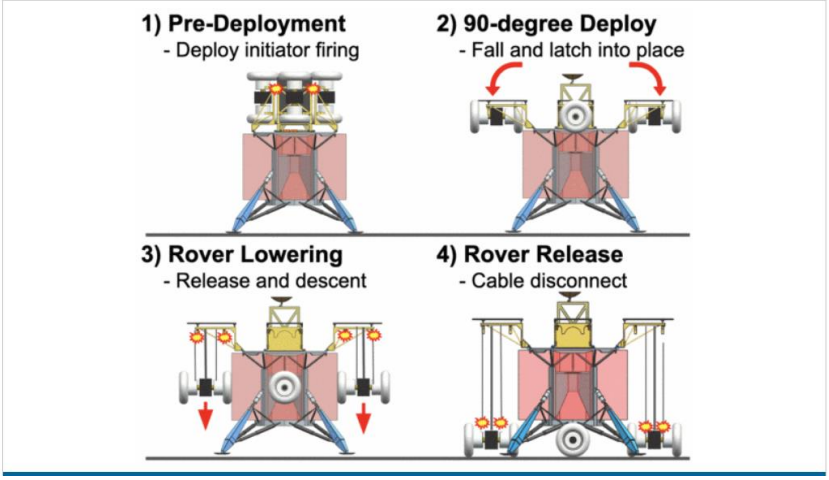

Figure 8: Tethered Rover deployment concept. [19]

The third concept is similar to the second concept and is called free-fall deployment. In this concept, the hanging rover is released without any tether or robotic arm to support its weight. The rover free-falls onto the lunar surface resulting in simpler deployment but high impact load and high risk of turn-over.

2.7 Existing Structural Analysis and Validation Methodology

2.7.1 Finite Element Analysis

Finite element analysis (FEA) is a key methodology for verifying the structural integrity of CubeSats. Yeon-kyu Park conducted a detailed finite element analysis of a 1U and a 2U CubeSat structural design, focusing on modal analysis, random vibration analysis, quasi-static loading, and thermal stress analysis to evaluate structural integrity and survivability in harsh space environments [20]. As an example, the CubeSat finite element model (FEM) by Yeon-kyu Park is shown in Figure 9.

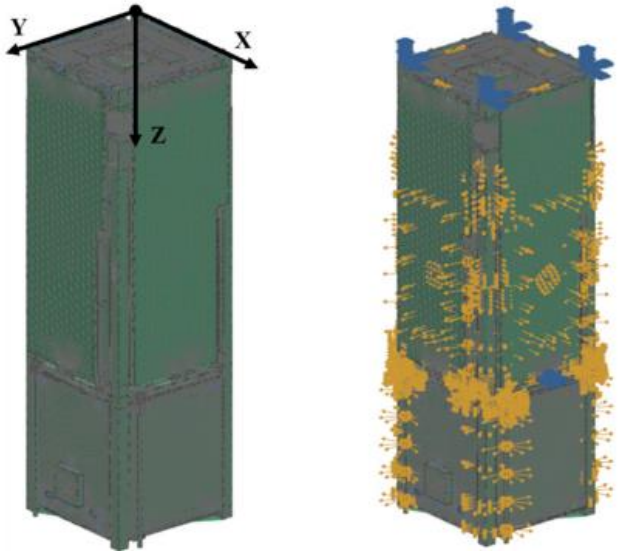

Figure 9: Finite Element Model of a 1U and a 2U Stowed in a 3U dispenser with contact and constraint conditions. [20]

Christopher also demonstrated how nonlinear explicit FEA using LS-Dyna can accurately predict impact loads on CubeSat structures during lunar surface landing [21]. For FEA model calibration, Majid conducted frequency response studies to calibrate finite element models, ensuring that predicted structural behavior aligns with experimental data [22]. This model calibration technique can be useful for calibrating CubeSat dynamic analysis model.

From literature review, the following analyses are essential, in order of importance, for CubeSat-based rover structural integrity check and will be conducted in this thesis:

1. **Shock and Impact Analysis** – Evaluates structural response under high-g impulse load during deployment and landing impact
2. **Modal Analysis** – Identifies the natural frequencies and mode shapes of the structure to avoid resonance during launch.
3. **Random Vibration Analysis** – Simulates the random vibrations experienced during launch to ensure components remain functional throughout the mission.
4. **Quasi-Static Analysis** – Evaluates structural response under high-g acceleration during launch.
5. **Thermoelastic Analysis** – Ensures structural performance under extreme thermal change in space.

2.7.2 Experimental Testing

Experimental testing is an important step in validating the structural performance of CubeSats and rovers for space missions. In addition to that, the test results are also critical for FE model calibration which is crucial in predicting structural performance of CubeSats outside of test scenarios. Yeon-kyu Park conducted sine and random vibration tests for 2U CubeSat using shaker table as shown in Figure 10 [20]. Five Accelerometers were used to measure structural response at various critical points in the form of acceleration. Quasi-static test was also simulated using sine burst profiles.

Figure 10: Vibration Test Setup example. [20]

Literature on experimental testing was initially explored with the intention of conducting experimental dynamic tests for FE model calibration. However, these tests were ultimately not performed due to limited time and budget for fabricating aluminium CubeSat-based rover structure.

2.8 Structural Analysis Theoretical Background

The theoretical background provided in this section largely draws upon the comprehensive knowledge presented by Jacob Job Wijker in "Spacecraft Structures" book [23]. This authoritative reference extensively covers the fundamental concepts and advanced techniques necessary for analyzing responses of structures.

2.8.1 Shock Response Spectrum Analysis Theory

Shock Response Spectrum (SRS) analysis characterizes peak dynamic response of a system to transient shock inputs, such as launcher stage separation or lander impact. The fundamental principle involves solving the governing differential equation for a damped single-degree-of-freedom (SDOF) system under base acceleration $\ddot{y}(t)$, shown in Equation (1):

$$\mathrm{m}\ddot{x}(t) + c\dot{x}(t) + kx(t) = -m\ddot{y}(t) \tag{1}$$

Where:

- x(t) is the relative displacement between the mass and the moving base,
- m, c, and k are the mass, damping coefficient, and stiffness of the system, respectively,
- $\ddot{y}(t)$ is the base acceleration input.

This differential equation is numerically integrated in the time domain for a range of natural frequencies representing multiple hypothetical SDOF systems. For each frequency, the peak absolute response (acceleration, displacement, or velocity) is extracted. By repeating this procedure over a frequency spectrum, an SRS curve is generated, which plots the maximum responses over a certain range of frequencies.

When evaluating the overall peak response of a structure, responses from multiple frequencies must be combined. In this report, the Square Root of the Sum of the Squares (SRSS) method is adopted to evaluate the SRS analysis results. The SRSS approach is commonly used in shock and vibration analysis when the input contains multiple modal responses that are uncorrelated. By combining the peak responses from each frequency mode using root sum square, the SRSS method provides a conservative yet realistic estimate of the total system response over a dynamic shock load profile ranging up to 10000 Hz. [24]

2.8.2 Modal Analysis Theory

Modal analysis determines the natural frequencies and corresponding mode shapes of the structure. Natural frequencies help determine whether there will be dynamic couplings with frequencies of launcher or lander vehicles. It also gives a measure of the structure stiffness. The natural frequencies can be determined through solving the equation shown in Equation (2).

$$(\mathbf{K} - \omega^2\mathbf{M})\emptyset = \mathbf{0} \tag{2}$$

Where $\mathbf{K}$ is the global stiffness matrix, $\mathbf{M}$ is the global mass matrix, ω is related to the natural frequency by $\omega = 2\pi\mathrm{f}$, and $\emptyset$ is the mode shape vector.

2.8.3 Random Vibration Theory

Random vibration analysis evaluates the response to statistically distributed vibrational load across a certain frequency range. These excitations are usually defined as Power Spectral Density (PSD) profiles, which define the intensity of acceleration (or force) as a function of frequency. The governing equation for random vibration analysis is the same as SRS analysis governing equation shown in Equation (1). The difference is in the base excitation, $\ddot{y}(t)$, input format. Instead of a shock spectrum, a stochastic power spectral density profile is inputted instead. Instead of tracking peak responses, random vibration analysis computes responses in terms of root mean square (RMS) values, allowing engineers to predict the probabilistic amplitude of vibration responses. [25]

2.8.4 Quasi-static Analysis Theory

Quasi-static analysis assesses the structural response to sustained inertial loads experienced during rocket launch. It assumes negligible dynamic effects and treats acceleration as a constant body force. Its governing equation of quasi-static analysis is shown in Equation (3)

$$\mathbf{Ku} = \mathbf{F} \tag{3}$$

Where $\mathbf{K}$ is the global stiffness matrix, $\mathbf{u}$ is the displacement vector, and $\mathbf{F}$ is the force vector, typically $\mathbf{F} = \mathrm{m} \cdot \mathrm{a}$ where a is the input g-load.

This equation forms the basis for evaluating displacement, which can then be used to calculate stress and margin of safety under worst-case acceleration loads.

2.8.5 Sensitivity Analysis Methods

Sensitivity analysis is a critical methodology in engineering analysis, aiming to evaluate the impact of input parameter variability on system output response. A variety of methods exist to perform this evaluation, ranging from variance-based sensitivity analysis to meta-modeling techniques that improve computational efficiency, such as the Metamodel of Optimal Prognosis.

In finite element modeling, sensitivity analysis is frequently applied to evaluate the impact of uncertainties in material properties, geometric tolerances, and boundary conditions, on structural or thermal responses. Sampling techniques such as Monte Carlo Simulation (MCS) and Latin Hypercube Sampling (LHS) are commonly used to explore the input space. [26]

After sampling input variables, sensitivity analysis is employed to quantify the influence of input parameters on model outputs. Among existing sensitivity analysis methods, the Metamodel of Optimal Prognosis (MOP) is a notable approach developed by Dynardo [26] for Ansys optiSLang software. MOP is a form of metamodel-based sensitivity analysis method which combines model-independent quality assessment (via the Coefficient of Prognosis, CoP) with automated variable selection to identify an optimal subset of influential parameters. It evaluates multiple approximation strategies, such as polynomial regression and Moving Least Squares (MLS), and selects the one that yields the best predictive performance in a reduced input subspace.

3 Methodology

This chapter describes the approach undertaken to design, simulate, and validate the structural, thermal, and mobility subsystems of the EMEC2 CubeSat-based rover.

3.1 Mechanical Design Approach

The CubeSat frame structure was designed to conform with the CubeSat Design Specification Rev. 14, while the rover was designed to accommodate selected mobility system concept and modular integration with a standard 3U CubeSat. CAD modelling was performed using Autodesk Fusion 360. The material selection focused on aerospace-grade aluminium for structural elements due to its high strength-to-weight ratio and compatibility with typical CubeSat construction.

3.1.1 Rover and Wheel Design

The EMEC2 CubeSat-Based Rover is designed for lunar surface mobility using a lightweight, rigid wheel with integrated grousers. Multiple concepts, including flexible wire mesh and spring-based hoops, were evaluated from literature on historical lunar rover wheel concepts [4]. Rigid wheel with grouser concept was selected for ease of manufacturing and integration simplicity. The mechanical architecture includes four independently driven wheels, each connected to a planetary gearbox and brushless DC motor, allowing for skid-steering and point-turning capabilities. The wheel grouser size and spacing were optimized for minimum mass with sufficient traction, based on analytical terramechanics models which will be explained with Equation (4) and (5). The CAD visualization in Figure 11, shows the overview of the rover design, illustrating how the wheel, chassis, and actuator components are integrated into a rover system.

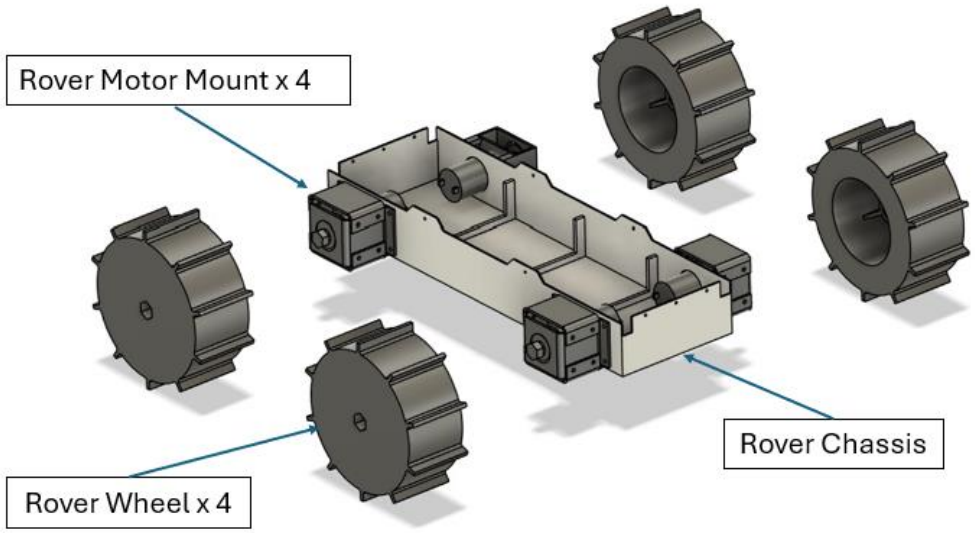

Figure 11: Exploded view of the latest rover subsystem showing the wheel, motor mount, and chassis structure.

Wheel thrust performance and torque requirement based on wheel dimensions were calculated using terramechanics equations for shear and normal stress distribution:

$$F_x = rb \int_{\theta_r}^{\theta_f} [\tau_x(\theta) cos\theta - \sigma(\theta) sin\theta] d\theta \quad (4)$$

$$T = \int_{\theta_r}^{\theta_f} r^2 b \tau_x(\theta) d\theta \quad (5)$$

where F_x is the net thrust, T is torque require, r is the wheel radius, b is the wheel width, and τ_x, σ are shear and normal stress components, respectively. θ_r and θ_f are the entry and departure angles, respectively, which define the angular extent of soil-wheel contact. To calculate normal and shear stress components, the soil properties and rover weight must be known in order to calculate stress distribution. Sample calculation can be further studied in the reference by Alhammadi [4].

With known lunar surface mobility requirements, such as transverse speed of around 5 cm/s and terrain slope of 45 degree, referenced from Alhammadi [4], and relations between wheel dimension and thrust, the wheel dimensions can be optimized for minimum mass while providing sufficient wheel thrust. A Python script for wheel performance analysis was developed to repetitively calculate for wheel thrust and torque require using Equation (4) and (5), based on wheel dimension input. Output results are compared with mobility requirements to ensure sufficient wheel thrust for lunar surface mobility with selected wheel radius and width. The wheel sizing python script can be studied in detail in **Appendix A**. Through iterative solving for minimum wheel mass, the resulting wheel dimension and performance is shown in Table 1.

Table 1: Final Wheel Design Parameters Summary

Parameter	Value	Unit
Wheel Diameter	110	mm
Wheel Width	50	mm
Wheel Grouser Height	8	mm
Wheel Thrust	12.5	N
Maximum Torque Required	0.40	$\mathrm{N \cdot m}$
Allowable Motor RPM range	6 - 12	RPM
Estimated Rover Speed	3.5 – 7.0	cm/s
Allowable longitudinal slope	45	deg

With known motor torque requirements from terramechanics analysis, space rated motor, Maxon ECX FLAT 22 L with GPX22 Planetary Gearbox, was selected as the wheel driver motor. Its model along with the motor driver module model is shown in Figure 12 below.

ECX FLAT 22L Motor [27]

GPX22 Planetary Gearbox [28]

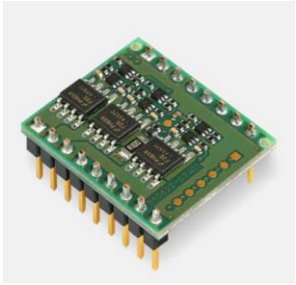

DEC Driver Module 24/2 [29]

Figure 12: Maxon ECX FLAT 22 L with GPX22 Planetary Gearbox Specification

The total mass of four sets of this motor drive system is estimated to be 0.50 kg.
To minimize structural mass while maintaining structural integrity, the rover chassis was initially designed to be constructed from Aluminium 6082-T6, a high-strength aerospace-grade alloy commonly used in CubeSat structures due to its favorable strength-to-weight ratio [30]. The material selection was further validated through finite element analysis under launch and landing load cases (to be discussed in Section 3.4.3). The rover wheels materials were selected addressing two critical challenges: abrasion resistance and thermal stability under lunar conditions. Polyether ether ketone (PEEK), a high-performance thermoplastic, was selected as the wheel material due to its resistance to lunar regolith abrasion, low thermal conductivity, and dimensional stability in vacuum and temperature extremes [31] [3].

With all dimensions related to rover systems determined, the detail design of each rover structural component was conducted. As previewed in Figure 11, the rover structure consists of three parts: Rover Motor Mount, Rover Chassis, and Rover Wheel. The CAD model of each part is shown in Figure 13.

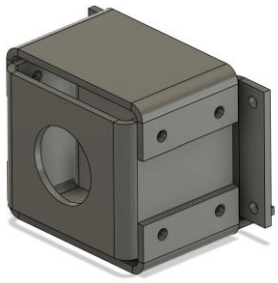

(a) Rover Motor Mount

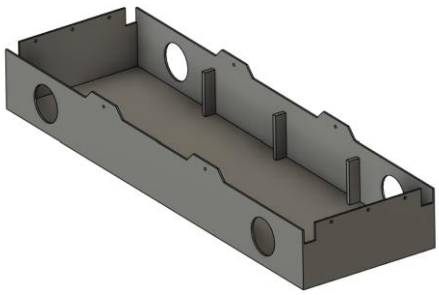

(b) Rover Chassis

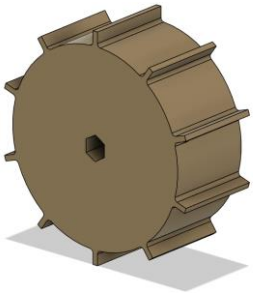

(c) Rover Wheel

Figure 13: Rover Structural Component CAD model

3.1.2 CubeSat-based Rover Mechanical Design

The structure design of EMEC2 CubeSat-based rover consists of two main components: the CubeSat component and the rover component. While the rover structure design is already shown in Rover and Wheel Design Section 3.1.1, its integration with the CubeSat's primary structure, which was designed by Pratheek [32] following the CubeSat Design Specification Revision 14 [9], is shown in Figure 14. The major difference from a standard 3U CubeSat structure is the addition of ten holes drilled on the CubeSat Side Frames and CubeSat End Frames, shown in Figure 14(a) and Figure 15, to accommodate interfacing with rover chassis component. A custom mounting solution was also designed, by Pratheek, to integrate non-CubeSat standard components such as the HYSPIM

camera payload. Standard CubeSat subsystem components from EnduroSat and AAC Clyde Space were selected for integration compatibility and modeled in Fusion 360. Subsystem components include battery, solar panels, attitude control, communication, and data handling systems. Component selection resulted in total mass of 6.5 kg for EMEC2 CubeSat-based Rover, later explained in detail in Result Section 4.1. All CubeSat structural components shown in Figure 14 are **initially** selected to be Aluminium 6082-T6 alloy due to its lower cost. This is later changed to Aluminium 7075-T6 and will be explained in Section 4.5.4. The rover structural components, as shown in Figure 11, are also initially selected to be Aluminium 6082-T6, with the exception of rover wheels which are made of Polyether ether ketone (PEEK).

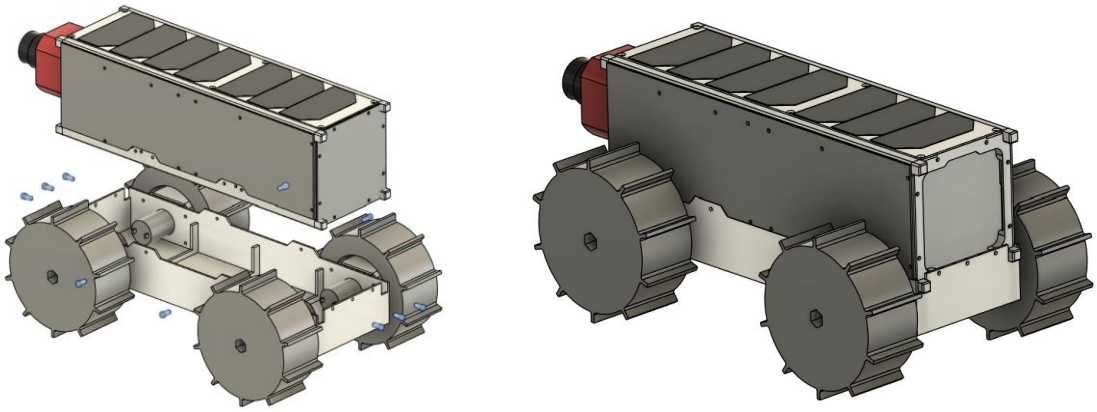

(a) EMEC2 CAD model: CubeSat above rover components

(b) EMEC2 CAD Assembled model

Figure 14: CubeSat-based Rover configuration overview: (a) Disassembled CubeSat, (b) Assembled Model

To go into more detail of each component in the EMEC2 rover assembly, an exploded view of the EMEC2 CAD model is shown in Figure 15. In order to prevent confusion between prototype and actual flight model design, the flight model design will be called Space Model, while the adjusted model for prototyping will be called Prototype Model.

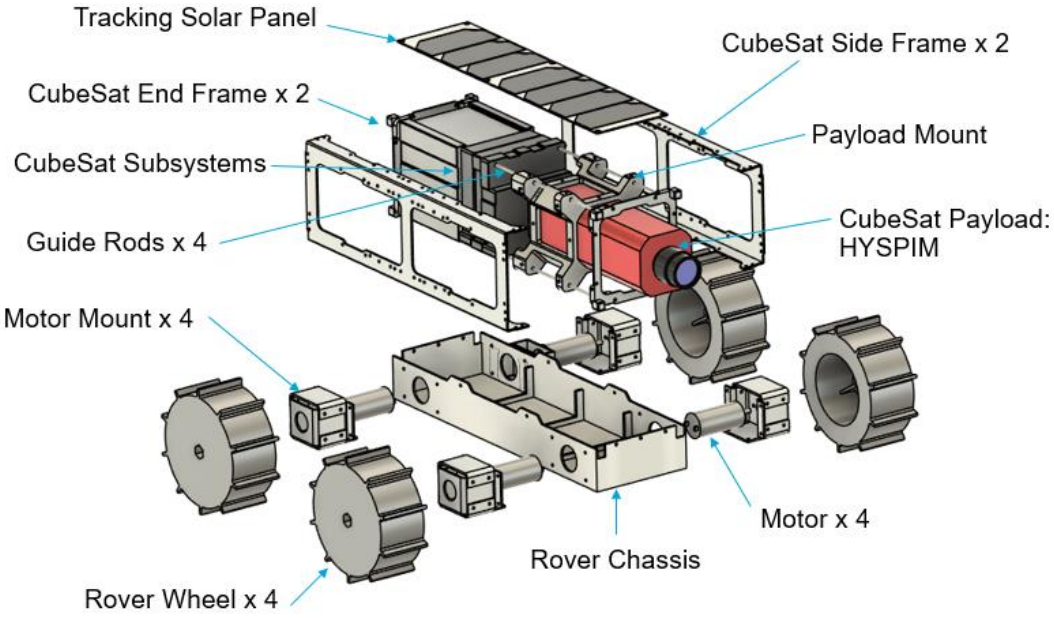

Figure 15: EMEC2 Space CAD Model: Exploded View

The primary structure of the CubeSat component comprises of CubeSat Side Frame and CubeSat End Frame which are 1.6 mm in wall thickness. Internal subsystem components and the payload mount are connected to the primary structure through four guide rods which go through each subsystem component, and end at CubeSat End Frame. The Rover Chassis is responsible for transferring loads to the rover wheels and interlocking the CubeSat with the rover system. Both the Rover Chassis and four Motor Mounts are initially 1.60 mm wall thickness aluminium alloy parts before design change.

3.1.3 Preliminary Assembly Validation using additive manufacturing

Due to the high cost of manufacturing aluminium structural components for the EMEC2 design, a preliminary verification of the structural assembly was conducted using a physical mock-up made from polylactic acid (PLA) plastic. In order to fabricate the mock-up model, a separate CAD model was created, called Prototype Model, and is shown in Figure 16, exploded view.

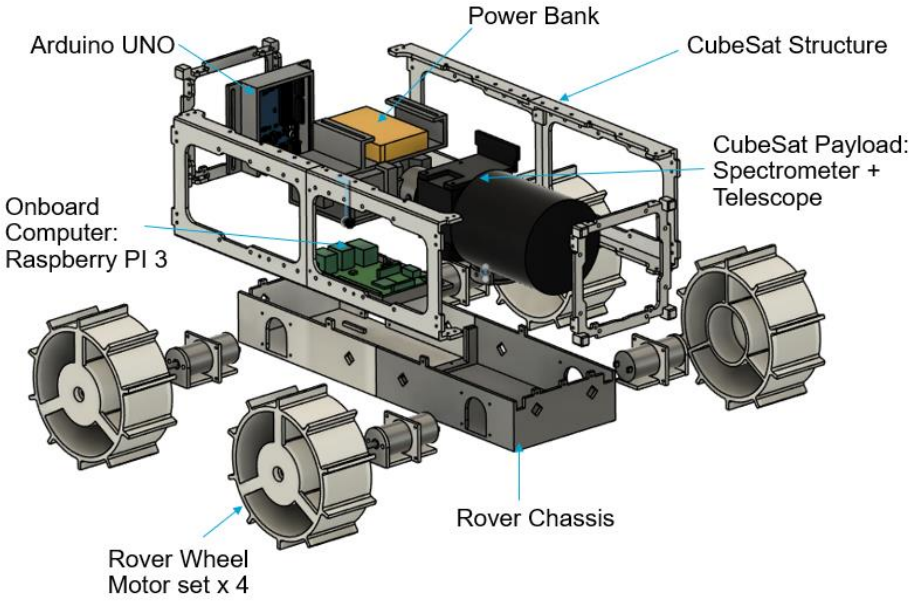

Figure 16: EMEC2 Prototype CAD Model: Exploded View

The mock-up structure, shown in Figure 17, was fabricated by the author using Prusa 3D printers available at Delft Aerospace Structures and Materials Laboratory (DASML). The parts were printed using PLA filament sourced from 123 3D B.V.

To ensure successful printing and allow for human handling, minor design modifications were implemented. These included increasing the minimum part wall thickness from 1.6 mm to 3.0 mm and segmenting larger components into smaller parts with additional fastener joints, due to the build volume limitation of the available Prusa MK4 printer (250 × 210 × 220 mm). The prototype served not only to validate mechanical fit and assembly but also to support preliminary system integration and interface testing.

Figure 17: Mock-up CubeSat-based rover structure assembly

3.1.4 Mobility Test Setup

To evaluate the mobility performance and verify the wheel sizing methodology of the CubeSat-based rover, a physical test was conducted using a 3D-printed rover prototype on a sandy beach terrain at Hoek van Holland, Delft. This test environment was selected due to its immediate availability and bulk density similarity of sand to lunar regolith according to David Carrier [33]. To go into more detail, Table 2 shows comparison between the properties between lunar soil and beach sand.

Table 2: Lunar regolith and Sand properties comparison

Soil Property	Surface lunar regolith	Dry beach sand
Average Particle Size (mm)	0.072	0.100 – 2.0
Coefficient of Uniformity	10 - 16	2 - 5
Bulk Density (kg/m^3)	1300 - 1800	1500 - 1700
Soil Cohesion (Pa)	100 - 1500	0 - 1000

While similar bulk density is shown, it must be noted that the difference in particle size, the lack of uniformity of lunar regolith, and the higher lunar soil cohesion from electrostatic interactions, make beach sand not entirely suited to simulate lunar regolith condition.

The rover prototype, with a total test mass of approximately 1.5 kg including onboard electronics, was equipped with four JGA25-370 motors with integrated gear reduction by Shenzhen Tianqu Electronics Co., Ltd, which provides 0.9 N・m torque at 12V and 12 RPM, meeting required torque and RPM from wheel analysis and rover speed requirement. Each motor was independently driven via an Arduino UNO microcontroller connected to two L298N dual H-bridge driver module. A custom Arduino script, developed by the author, controls the motor actuation. The Arduino code is provided in **Appendix B**.

Both static and dynamic sinkage tests were performed. Static tests were conducted by lifting the rover just above the sand surface and placing the rover down. Dynamic tests involve driving the rover forward remotely and measuring sinkage from the immediate wheel footprint.
For each condition, the vertical distance from the wheel axle to the lowest point of the sand surface was measured using a digital vernier caliper with 0.01 mm resolution. The measurement is repeated ten times, and the average value is reported. Figure 18 illustrates the deployed prototype on the test site.

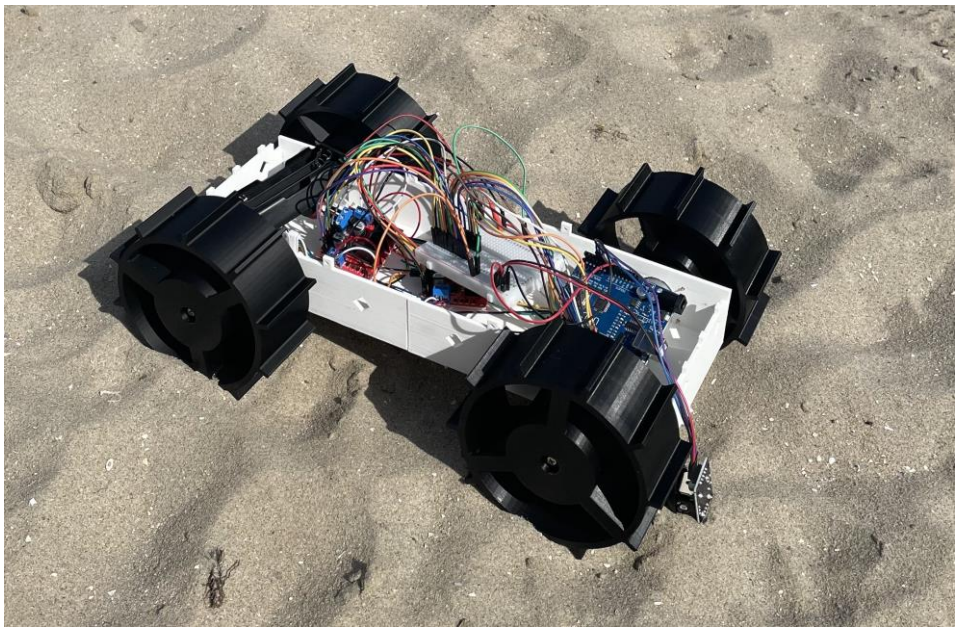

Figure 18: Wheel mobility test setup using mock-up rover system at Delft's Hoek van Holland beach

This setup enabled a preliminary validation of terrain traversability and wheel-soil interaction analysis model. The validation involves comparing the sinkage result between analysis and experiment, presented later in the report Section 4.2.

3.2 Thermal Design Approach

The EMEC2 CubeSat-based Rover will experience two different phases of extreme thermal environment: Moon Lagrange-2 orbit phase, and Moon surface exploration phase. The CubeSat-based rover design must be able to withstand rapid temperature changes during these phases, including eclipse periods and prolonged exposure to direct solar radiation and moon surface temperature.

Given the limited mass and power budgets of a 3U platform, passive thermal control was prioritized. The design utilizes multilayer insulation (MLI), with typical effective emissivity of 0.03 and typical conductivity of 0.5 $\frac{W}{m^2 \cdot K}$, as referenced from Spacecraft Thermal Control Handbook [34]. MLI is used to contain heat within the spacecraft during eclipse period, and passive radiation is used to radiate heat out during long-term sun exposure. All subsystems were considered during the design process and in the thermal model. The summary of thermal load and thermal optical properties used for the CubeSat-Based Rover is summarized in Table 3.

Table 3: EMEC Thermal Load and Thermo-optical Properties [34]

Subsystem	Maximum Power Consumption (W)
Hyperspectral Camera	12
Four Drive Motors	16
All Other Subsystems	10

Component	Absorptivity (α)	Emissivity (ε)	Reference
Solar Panel Cover Glass	0.9	0.85	[35]
External Surface Black-Anodized Aluminium	0.9	0.80	[36]
Internal Surface White Paint	0.2	0.80	[36]
Solar Cell Surface	0.95	0.80	[37]
Lunar Regolith Surface	0.88	0.90	[38]

3.3 Thermal Model Setup

3.3.1 In-orbit Thermal Model

For EMEC2 mission, orbital analysis by Alex Rinon [39] has shown that the maximum possible eclipse duration throughout the mission is approximately 25 minutes based on possible similar to trajectory shown in, excluding Lunar night. The worst-case 30-minutes eclipse scenario was used to assess spacecraft survival without sunlight. The orbit used to simulate the 30-minutes eclipse scenario is an elliptical orbit shown in Figure 19 below.

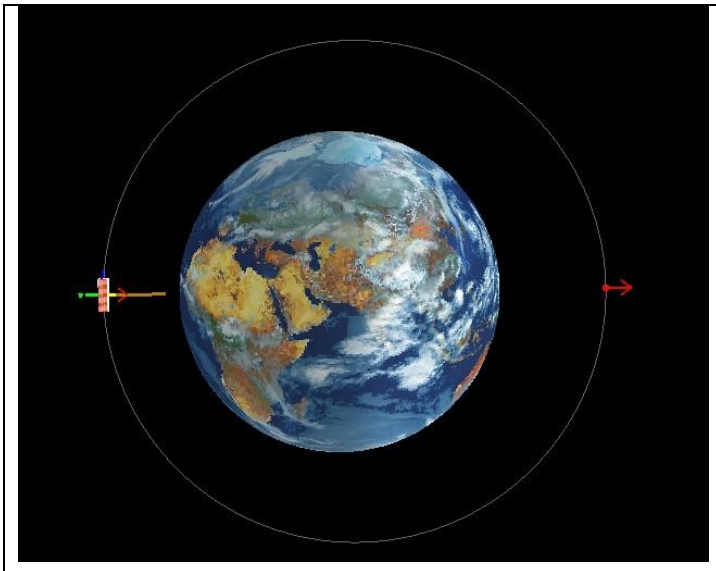

Minimum Altitude	3000 km
Eccentricity	0.06
Orbit Inclination	117.96°
Argument of Periapsis	0°
Local Time at Ascending Node	0:00:00
Solar Declination	0°

Figure 19: Elliptical Orbit, simulating Eclipse Duration of 30 Minutes

The thermal model is simplified to only CubeSat component as shown in Figure 20.

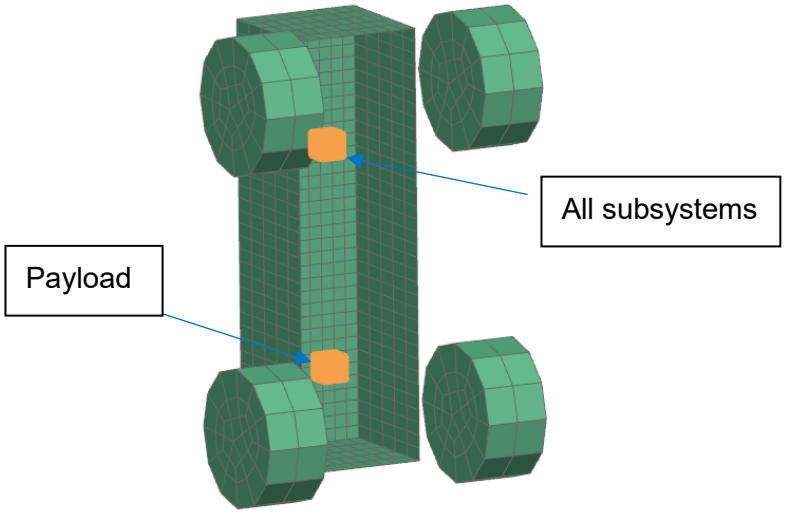

Figure 20: Simplified In-orbit Thermal Model

Subsystem components are simplified into two small nodes in the middle of the CubeSat panel, one for the HYSPIM payload and another for all other subsystem components bundled together. Thermal conduction between CubeSat structure and subsystem components are assumed to be negligible as thermal isolation element is planned to be applied to the mounting. Heat transfer between the nodes mainly through radiation. Thermo-optical properties and thermal loads, as discussed in the previous Section 3.2, were applied to the respective parts of the model. It must be noted that black thermo-optical properties are applied to all external surfaces, including the wheels, with the exception of solar panel surface.

3.3.2 Lunar Surface Thermal Model

The lunar surface environment is known for its extreme thermal conditions, with a surface temperature reaching up to 127℃ during lunar day [3], which is EMEC2 total time of operation. A solution for EMEC2 to survive lunar nights within the given mass and volume budget was not discovered. Based on preliminary thermal simulation of lunar night, a continuous power source must be provided for 14 days to survive lunar nights which require power budget of approximately more than 10,000 Wh which equates to more than 10.0 kg of mass budget. The models evaluated component temperature range in full-load condition, where components operate at maximum power consumption, and idle-load conditions, where components are assumed to passively consume 1 Watts each, rounded up from components' specification on idle mode power consumption. Solar Heating was also applied to the CubeSat-Based rover for its entire mission lifetime of 14 days on the lunar surface. Simplified EMEC2 CubeSat-Based model, used for thermal simulation, is shown in Figure 21.

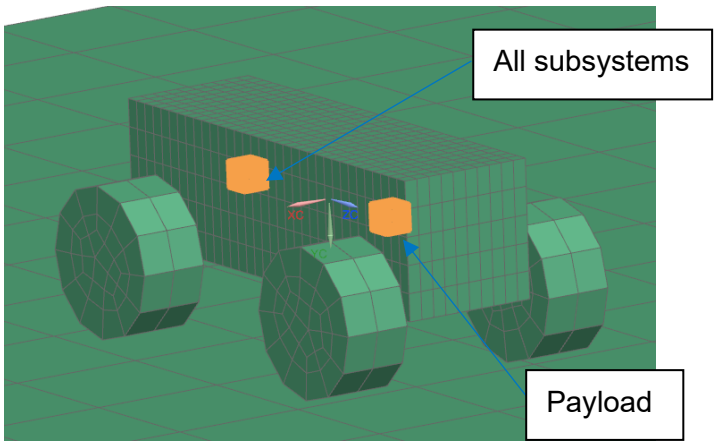

Figure 21: EMEC2 Lunar Surface Thermal Model.

In addition to radiation, thermal conduction is also dominant in lunar surface thermal simulation. Convection is, however, still negligible. Through the result convergence study, the lunar surface size dimension was modeled to be five times larger than the rover length in order accurately simulate the view factor of lunar surface.

3.4 Structural Analysis Model Setup

Finite element (FE) modelling of the CubeSat-based Rover structure was performed in NX Simcenter finite element analysis software using combinations of 2D quadrilateral mesh sheet elements, 3D tetrahedron solid elements, and 1D beam elements, with point masses representing internal components as shown in Figure 22(a). The entire FE model consists of 65000 2D quadrilateral Aluminium 7075-T6 elements, 100000 3D tetrahedron solid Aluminium 7075-T6 elements, 665 1D elements, and 6 point masses. Point masses include hyperspectral camera payload, four motors plus wheels masses, and CubeSat subsystem components bundled together. The total number of nodes is approximately 115000 nodes. 1D bar element AISI 304 Steel fasteners are used to connect parts together, along with frictional contacts used between aluminium parts with friction coefficient of 1.0 according to Wang [40].

Through the boundary condition highlighted in Figure 22(b), excitations are applied for random vibration and shock response spectrum analysis using acceleration profiles to be shown in Section 3.4.3. For quasi-static analysis, fixed boundary conditions are applied at the highlighted boundary, and gravitational field is applied accordingly. The initial FE model of CubeSat-Based rover is shown in Figure 22.

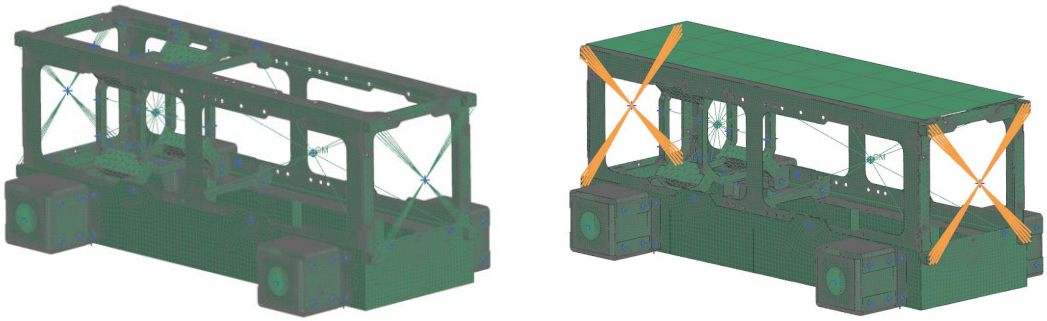

(a) Simplified model for FE analysis (b) Boundary conditions Highlighted

Figure 22: FE model setup: (a) Simplified geometry without panel, (b) Applied boundary conditions in orange.

Design changes were later implemented to this initial model for the structure to pass structural integrity requirements. The details will be explained in Section 4.5.4.

3.4.1 Material Properties

In order to perform structural analysis, it is crucial to clearly define the properties of each material used. Mechanical and thermal properties of all structural materials used in the EMEC project are summarized in Table 4.

Table 4: Mechanical and Thermal Properties of Selected Materials

Property	**Al 6082-T6**	**Al 7075-T6**	**PEEK**	**AISI 304 Steel**
Density, ρ $[kg/m^3]$	2700	2810	1320	8000
Modulus of Elasticity, E [GPa]	69	71.7	3.6	193
Poisson's Ratio, v	0.33	0.33	0.38	0.29
Ultimate Tensile Strength, σ_U [MPa]	330	572	90	520
Tensile Yield Strength, σ_Y [MPa]	270	503	90	205
Thermal Conductivity, k $[W/m \cdot K]$	160	130	0.25	16.2
Specific Heat Capacity, c $[J/kg \cdot K]$	900	960	1250	500
Thermal Expansion, α $[\times 10^{-6}/K]$	23	21.5	47	17.2
Reference	[41]	[30]	[31]	[42]

Critical damping coefficient of the entire system is assumed to be 5%, referencing ESA standard Mechanical shock design and verification handbook [24] for typical damping value of metal structure when performing SRS analysis. It must be noted that, technically, the exact damping coefficient should be tuned using experimental results if possible.

3.4.2 Margin of Safety

In structural analysis, the Margin of Safety (MOS) is a parameter used in many engineering fields to determine whether a system can withstand mechanical loads after accounting for various uncertainties. The methodology for calculating MOS in the scope of

the present work is specific to that of spacecraft design [43]. For any particular load case being analyzed, the value of MOS calculated in the following equation shall always be positive:

$$MOS = \frac{DA}{LL \times FOS} - 1 \quad (6)$$

The Design Allowable (DA) is the statistically based strength capability of the material with respect to failure modes.

The Limit Load (LL) is the maximum load that CubeSat structures are expected to experience during a specified loading environment. The maximum von-Mises stress observed in an FE analysis for a particular load case is usually taken as the LL.

The Factor of Safety (FOS) is applied to the Limit Load (LL) to account for uncertainties in material properties, manufacturing processes, and the verification approach. According to Spacecraft Design Standard ECSS-E-ST-32-10C [43], FOS can be calculated using Equation (7):

$$FOS = FOSY \times KQ \times K_M \quad (7)$$

Where:

- KQ is the qualification test factor applied for spacecraft to survive qualification test campaigns. A typical value of 1.25 is used for satellite according to ECSS-E-ST-32-10C standard [43].
- K_M is the model factor applied to account for FE model uncertainties. A typical value of 1.10 is used based on similar CubeSat satellite missions such as ISTsat-1 [44], and also based on Sensitivity analysis results in Section 4.7.3.
- $FOSY$ is the yield strength factor of safety applied to lower the probability of stress reaching material yield point. A typical value of 1.10 is used for satellite according to ECSS-E-ST-32-10C standard.

3.4.3 Structural Loads

Throughout the various mission phases from Earth to the lunar surface, the CubeSat-based rover must be designed to withstand the environmental loads from the launcher, space environments, and moon lander vehicle. In this study, the load cases from four possible launch vehicles — Falcon 9, Electron, Ariane 6, and Vega-C, were compared with the loads specified for the Peregrine lunar lander [1] [2] [45] [46] [47]. Vibration and Shock Response Spectrum profiles from Penegrine Lander, which is more severe than conventional launchers, are compared and shown in Figure 23 below:

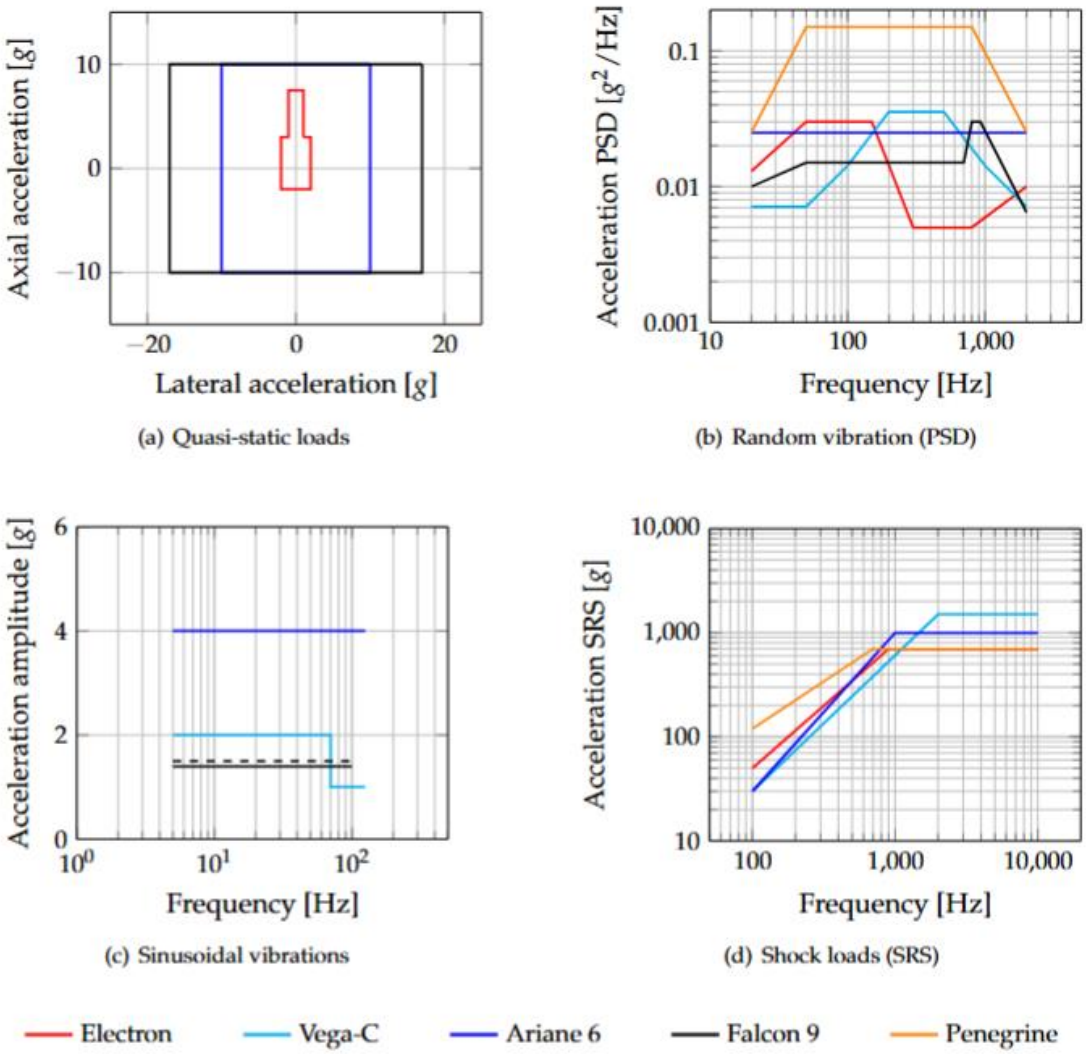

Figure 23: Critical load environments affecting the CubeSat-based Rover: (a) Quasi-static acceleration envelope, (b) Random vibration PSD, (c) Sinusoidal vibrations, and (d) Shock response spectrum.

Aside from structural loads, a minimum first-mode natural frequency requirement of 115 Hz is also adopted to satisfy the most stringent requirement across commonly used launch vehicles, including Ariane 6, Vega-C, Electron, and Falcon 9.

Lastly, thermoelastic analysis is also required to evaluate stress due to expansion and contraction of structural parts from temperature change. The temperature profile will be taken from the thermal analysis results in Section 4.3. For example, based on Figure Figure 25, the average temperature of each CubeSat panel is applied to CubeSat Side Frame, CubeSat End Frame, and their respective panels. The payload temperature is applied to the payload mount. The surface facing panel's average temperature is applied to the entire rover chassis and motor mount structures. PEEK wheel is assumed to be thermally isolated and has negligible mechanical effect on the rover structure when performing thermoelastic structural analysis. This assumption is made based on the low thermal conductivity shown in Table 4 and the mechanical clearance design feature involved in allowing rover wheel to turn in both contraction and expansion conditions.

3.4.4 Assumptions and Limitations

The methodology assumes idealized rigid boundary conditions, infinitely stiff rigid connection element between structure and subsystems, and subsystem components' structure not being modelled in the simulation. Thus, stress values at boundary conditions and subsystem component connection points will be abnormally high due to artificial stress concentration riser from rigid element used for these connection points. In addition, 2D simplification of some parts, such as Rover Chassis and Side Frames, introduce sharp corners without fillets. These also introduce stress concentration, or even stress singularity points. Local average will be used when addressing these stress concentration points. PEEK wheels are assumed to have negligible stress during critical load cases due to their relatively lightweight and its position in the load path. 20℃ baseline reference temperature is assumed for thermoelastic analysis, referencing ECSS standard [48].

3.5 Structural Model Validation Method

The structural model of the CubeSat-based rover was validated using **synthetic data** rather than experimental results. This approach was chosen to enable early-phase verification of the model under FE simulation conditions, in the absence of project budget for full-scale hardware testing. The synthetic data was generated using a high-fidelity reference finite element model, constructed independently with a slightly perturbed set of input parameters to simulate realistic design variability and manufacturing tolerances. The set of input parameters used is shown in Section 4.8 alongside tuned FE model result.

Key parameters used in generating the synthetic dataset include:

- **Young's Modulus of Aluminium** (used in both the CubeSat main frame and deployable rover substructures)
- **Structural Wall Thicknesses** (for CubeSat rails, side panels, internal mounting brackets, and rover structural components)
- **Total Mass** of the integrated system (including payload and mobility system)
- **Young's Modulus of Steel** (used for fasteners)
- **Poisson's Ratio** of both aluminium alloy and steel

These parameters were chosen based on the final CubeSat-based rover design specifications and materials selected for the flight model, as outlined in Section 3.4.1.

The synthetic reference model was used to extract modal responses, including natural frequencies and mode shapes.

The primary structural model of the CubeSat-based rover, with a certain baseline input parameter value, was then evaluated against the synthetic result. In order to tune the primary structural FE model to have the same modal frequency response as the synthetic result, Simcenter Design Space Explorer optimization module is used. The objective function defined for the optimization module is shown in (8).

$$\mathbf{J} = \sum_{i=1}^{n} w_i \left(\frac{f_i^{FEM} - f_i^{target}}{f_i^{target}} \right) \tag{8}$$

Where:

- $\mathbf{J}$ = total objective function value that is to be minimized.
- n = number of modes considered
- f_i^{FEM} = i-th mode natural frequency from FEA
- f_i^{target} = i-th target natural frequency
- w_i = weighting factor for mode i, which can be manually input based on importance

Using this objective function, the optimization module optimizes the FE model to have minimum error between the first four mode natural frequencies of the synthetic data, as the target, and the FE model. To achieve this, the key parameters are varied with their ranges, which are potential real-world physical variation determined through literature reviews, as specified in Table 5 below:

Table 5: Key input parameters variation range in optimization module.

Input Parameter	FE model Design Baseline Value	Value range	Reference
Aluminium Modulus (GPa)	70	68 – 76	[49]
Aluminium Poisson's Ratio	0.32	0.30 – 0.35	[49]
Aluminium Thickness (mm)	2	1.8 – 2.2	[50]
Total Mass (kg)	6.5	5.85 – 7.15	[51]
Steel Modulus (GPa)	200000	180000 – 220000	[49]
Steel Poisson's Ratio	0.28	0.26 – 0.30	[49]

Although this method does not replace experimental validation, the use of synthetic data provides an easily accessible means to verify the physical plausibility and numerical stability of the structural model.

4 Results

4.1 EMEC2 System Design Summary

The finalized mass distribution of the EMEC2 CubeSat-based rover system is shown in Table 6. This breakdown accounts for both the 3U CubeSat module and the rover platform, detailing individual subsystem contributions toward the total system mass. The specifications of each subsystem component are specified in the reference column.

Table 6: EMEC2 CubeSat-based Rover Mass Breakdown Summary

Component List	Mass (kg)	Reference
Hyperspectral Camera Payload	1.10	[52]
Communication System	0.50	[53], [54], [55], [56]
Battery + Power Distribution Unit	1.40	[57]
Solar Panel	0.60	[58]
CubeSat Structure	0.70	-
On-board Computer	0.20	[59]
EMEC 2 CubeSat Total	4.50	
Rover Structure	1.50	-
Rover Motor System	0.50	[27], [28], [29]
Rover Total	6.50	

The total mass of the entire system is **6.50 kg**, with the CubeSat platform accounting for **4.50 kg** and the rover subsystem contributing **2.00 kg**. These values were used to cross check with structural FE model point masses and structural masses.

4.2 Mobility System Testing Results

With the setup explained in Section 3.1.4, the 1.50 kg rover mobility system was tested under both static and dynamic conditions. Measurements were taken to quantify the sinkage of the wheels when the rover was stationary (static sinkage) and while in motion (dynamic sinkage). From the measurement results, Static sinkage was observed to be approximately 7.5 mm. Under dynamic conditions, sinkage increased to 13 mm, attributed to additional forces during wheel rotation, soil displacement, and slippage effect. Table 8 compares the field sinkage result to the analysis result from the wheel sizing analysis code when weight is increased to 14.7 N due to Earth's gravity.

Table 7: Comparison between analysis and field test wheel sinkage results

	Analysis Result	**Field test result**	**% difference**
Static Sinkage	6.70 mm	7.50 mm	11%
Dynamic Sinkage	14.15 mm	13.0 mm	9%

While the wheel normal force is not exactly representative of EMEC2 on lunar surface, validation of analysis method was achieved through comparing field test sinkage and motor torque results with analysis result using sand mechanical properties. The field test revealed consistent traction with the terramechanics model predictions under beach sand surface. The wheels generated sufficient thrust to propel the rover forward without significant slippage.

4.3 Thermal Simulation Results

4.3.1 In-orbit Thermal Simulation Result

The thermal simulation results for orbital simulation with 30-minute eclipse duration are shown in Figure 24.

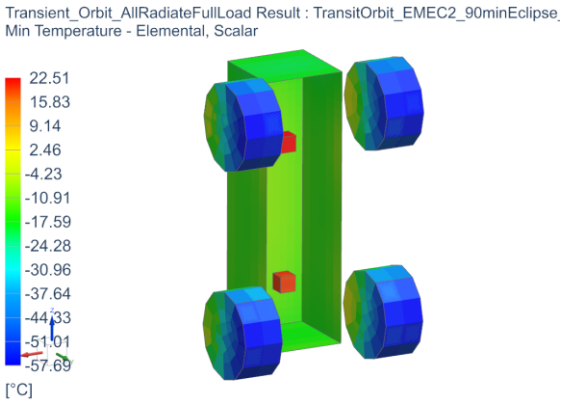

(a) Minimum Temperature Profile

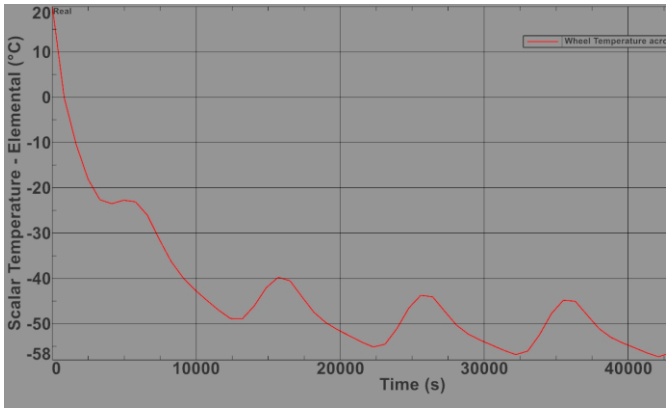

(b) Wheel Temperature over time.

Figure 24: In-orbit Thermal Simulation Results

During the 30-minute eclipse period, the temperature of the CubeSat Structure can cool down to around -60℃, especially the rover wheel not facing the sun during the sunlit phase. The payload and other subsystem components manage to stay above -10℃, which is well within their operating temperature range. It must be noted that the CubeSat-based rover will be accompanied with a Lunar lander which can provide improved thermal control system. This analysis is performed to demonstrate the worst-case scenario where no additional protection is provided to the CubeSat-based rover design.

4.3.2 Lunar Surface Thermal Simulation Result

The thermal simulation results for lunar surface environmental conditions are shown in Figure 25.

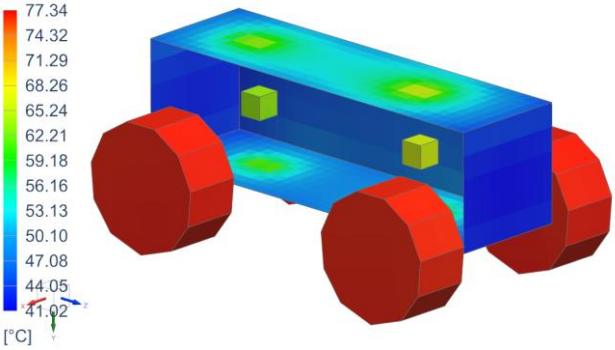

(a) Full Load Temperature Contour [℃] (b) Idle Load Temperature Contour [℃]

Figure 25: Lunar Surface thermal simulation results at different loads (a) Full Load (b) Idle 1 W Load.

At full load, the maximum temperature of the camera payload and other internal components of the spacecraft subsystem is approximately below $+65℃$ and above $-20℃$. The solar panel and structure panel temperature ranges start from $-20℃$ and ended up at most $+70℃$. The wheel temperature ranges from $+35℃$ to $+80℃$, which is acceptable as the ECX 22L motor inside the wheel has an operating temperature range from $-40℃$ to $+100℃$.
These values of temperature profile were then used to analyze the structural deformation due to temperature change from a reference temperature of 20℃ in the thermoelastic analysis shown in Section 4.5.4.

4.4 Structural FE model Mesh Convergence Study

Before assessing the structural analysis result, a mesh convergence study was conducted to ensure numerical stability and accuracy of the finite element results for the EMEC2 structure. Two representative load cases were used for evaluation:

- **Quasi-static load case**: Maximum von Mises stress was monitored across different mesh sizes.
- **Modal analysis**: First mode natural frequency was used as a metric to assess the impact of mesh refinement on dynamic behavior.

Figure 26 shows the reference finite element model used during the mesh convergence study, which is the updated model. The structure was meshed with varying global element sizes from 4.0 mm down to 2.0 mm, and both stress and modal outputs were recorded. A separate local mesh size convergence study was also conducted for local mesh around fastener holes, and the converged local mesh size control is already applied for the model in Figure 26.

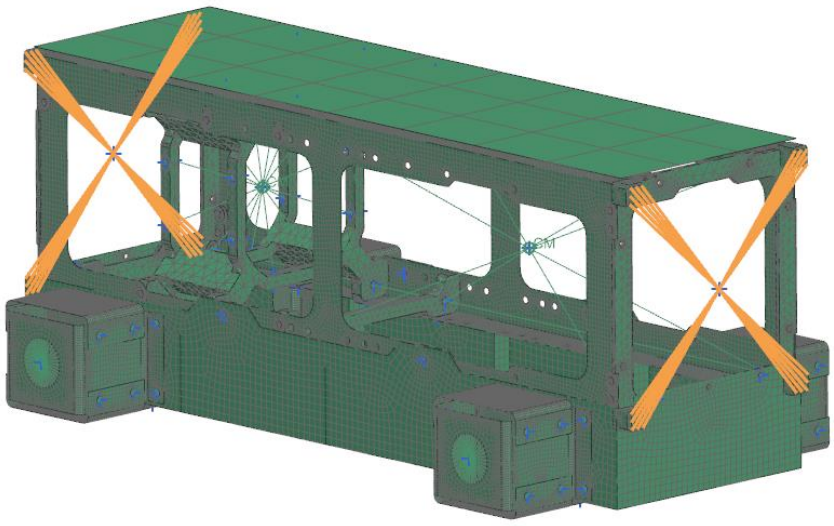

Figure 26: Mesh Convergence Study Reference Model

The convergence trends are presented in Figure 27. As the mesh was refined, the first mode natural frequency showed marginal variation, stabilizing around 500 Hz. Meanwhile, the maximum von Mises stress initially increased due to better resolution of local stress concentrations, then plateaued as mesh size decreased further. These results suggest that the solution had sufficiently converged at mesh sizes of 3.0 mm or below.

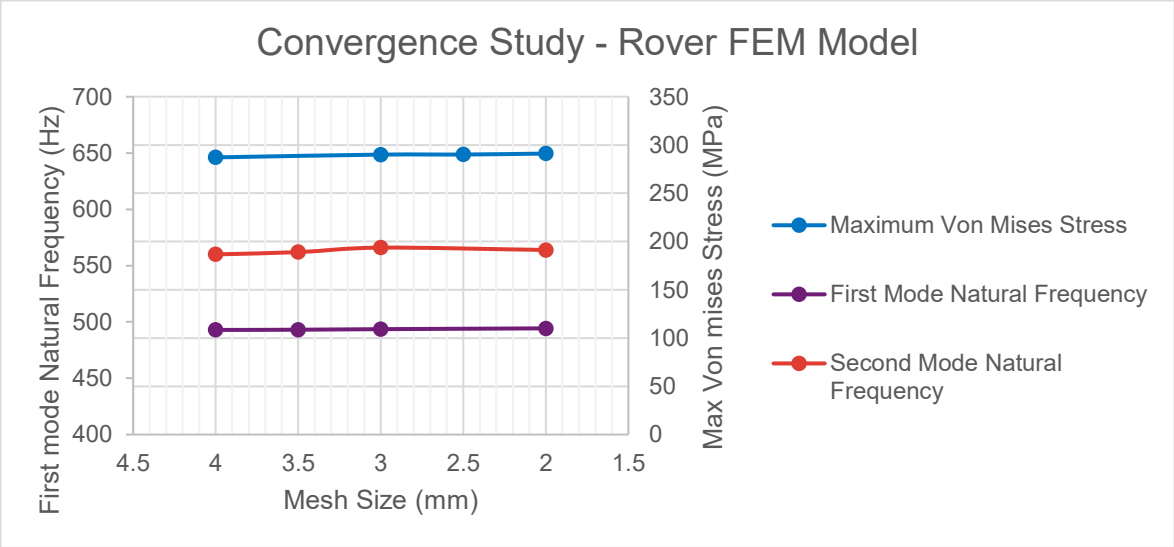

Figure 27: Mesh Convergence Study: Maximum Von mises stress and First Mode Natural Frequency

This study confirms that the selected mesh size of 3.0 mm provides a reliable balance between computational efficiency and result accuracy for both static and dynamic structural assessments.

4.5 Initial Structural Simulation Results

4.5.1 Quasi-static Analysis Result

The quasi-static load case simulates the peak accelerations experienced during launch as shown in Section 3.4.3. The most severe load case is from the combination quasi-static load case of +17g X-axis, +17g Y-axis, and +10g Z-axis. The resulting stress distributions are shown in Figure 28.

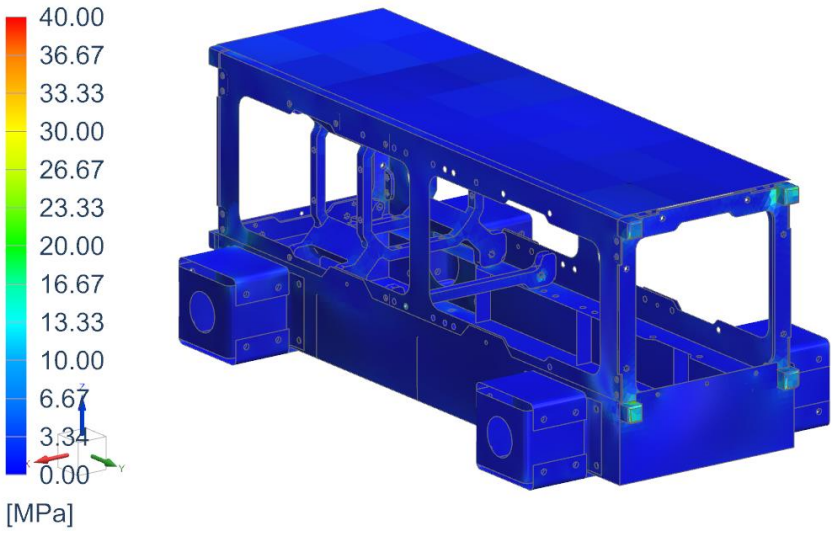

Figure 28: Quasi-static Analysis result: von Mises Stress contour.

The maximum von Mises stress observed was **40 MPa**, which occurred at the CubeSat End Frame part.

The material used for the initial design primary structure is Aluminium 6082-T6, which has a yield strength of **250 MPa**. This yields a minimum margin of safety (MoS) of **3.10** under the worst-case quasi-static loading condition.

4.5.2 Random Vibration Analysis Result

The most critical random vibration load case corresponds to the Z-axis direction of the Penegrine Lander random vibration profile. The RMS stress contour of the most severe case is shown in Figure 29.

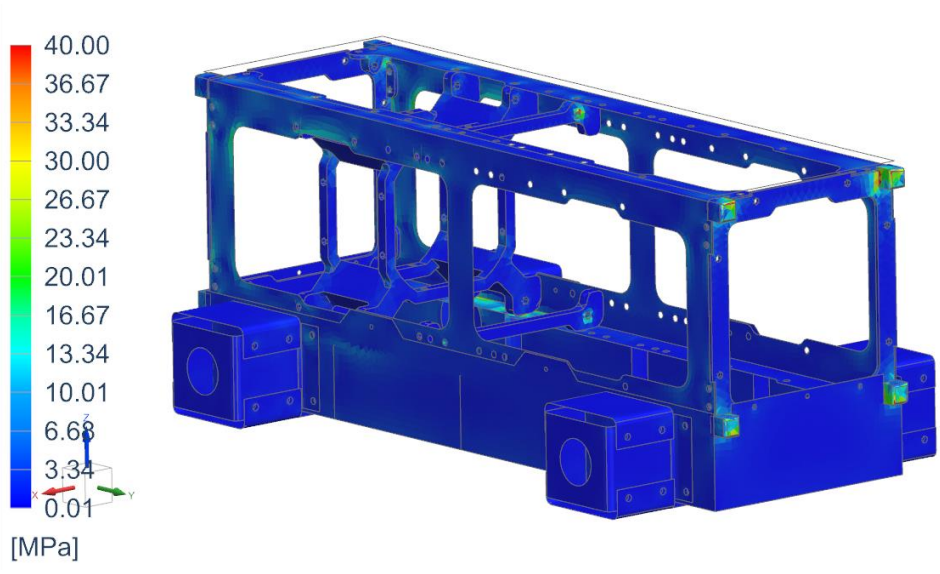

Figure 29: Random Vibration Analysis RMS von Mises Stress contour.

The computed RMS stress was **40 MPa**. Assuming a Gaussian probability distribution of random vibration analysis, the 3-sigma stress value, representing a 99.7% probability envelope, would be 120 MPa. This yields a minimum MoS of **0.38** under random vibration load cases.

As part of random vibration analysis, modal analysis was also conducted to determine natural frequencies of the model, screening from 10 Hz up to 2000 Hz. The first and second mode natural frequency of the structure was found to be **500 Hz and 570 Hz**, as shown in Figure 30, exceeding the 120 Hz minimum requirement imposed to avoid coupling with launcher dynamics.

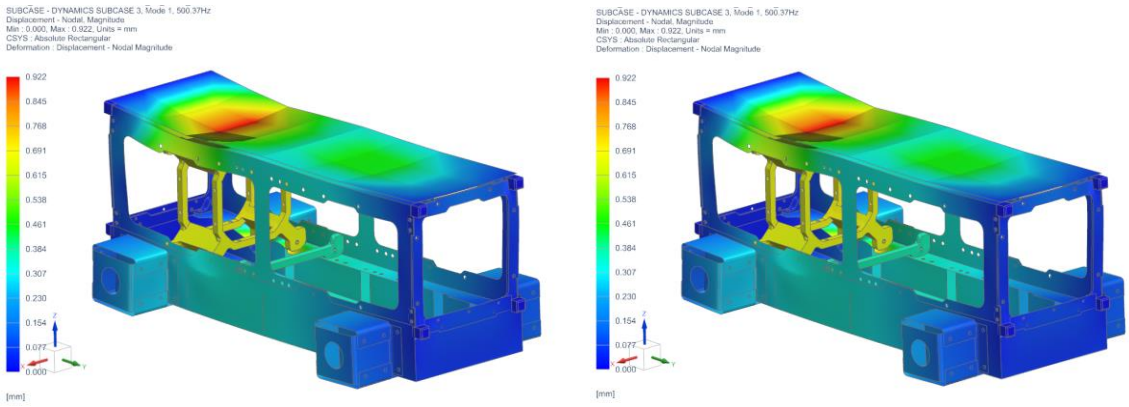

(a) First mode Frequency: 500.0 Hz (b) Second mode Frequency: 570.0 Hz

Figure 30: Modal Analysis results: First and second mode natural frequencies.

4.5.3 Shock Response Spectrum Analysis (SRS) Result

The most severe load case for SRS analysis is the Z-axis shock from Penegrine Lander Shock profile. The peak von Mises stress contour of this most critical case is shown in Figure 31.

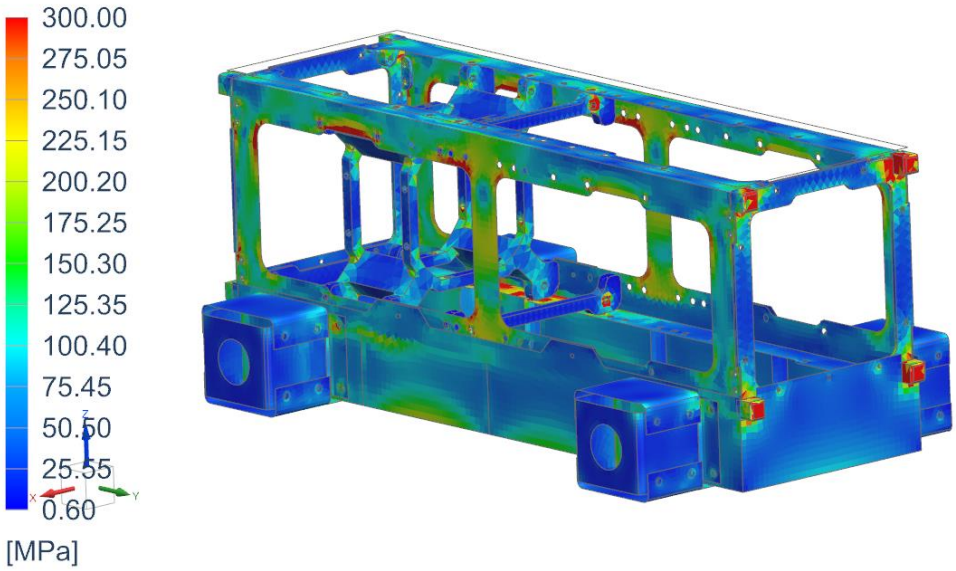

Figure 31: Shock Response Spectrum Analysis peak von Mises Stress contour: Initial Rover FE Model.

The peak Mises stress observed was **350 MPa**, which occurred at the CubeSat End Frame and Side Frame parts.

The material used for the initial design primary structure is Aluminium 6082-T6, which has a yield strength of **250 MPa**. This yields a negative margin of safety of **-0.50**, resulting in the yielding of the structure. Based on the shock analysis result, the design needs to be revised to pass the structural requirement under shock load.

4.5.4 Thermoelastic Analysis Result

The thermoelastic load case simulates the maximum temperature difference that can occur throughout the mission phases as shown in Section 4.3. The most severe load case occur when using the temperature profile from the Full Load operation on lunar surface shown in Figure 25a. The resulting stress distributions are shown in Figure 32.

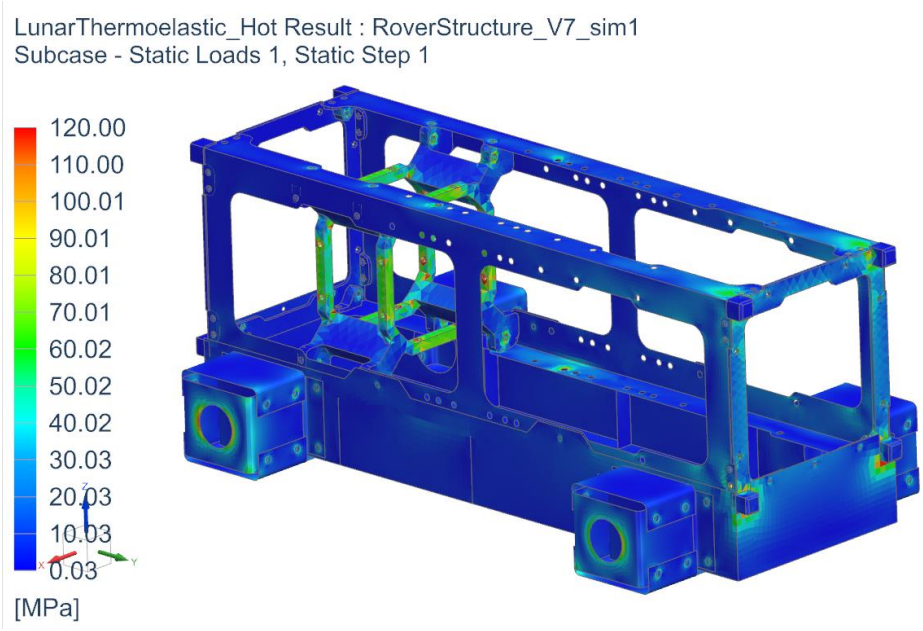

Figure 32: Thermoelastic Analysis Hot Case Result: Von Mises Stress

The maximum von Mises stress observed was **120 MPa**, which occurred at the Payload Mount part.

The material used for the initial design primary structure is Aluminium 6082-T6, which has a yield strength of **250 MPa**. This yields a minimum margin of safety (MoS) of **0.38** under the worst-case thermoelastic load condition.

4.5.5 Design Change

Initial simulations identified areas of stress concentration, particularly near sharp corners and fastener interfaces. As a result, several design modifications were implemented:

- Chamfering and filleting of internal corners to reduce stress risers.
- Increased thickness of the Rover Chassis and the four Motor Mounts from 1.6 mm to 2.0 mm to mitigate localized overstress.
- Reinforcement ribs were added to the rover chassis to enhance stiffness and increase first mode natural frequency.
- Lunar lander mounting structure design were added to introduce a more realistic contact and boundary conditions to the model. The design was based on Penegrine Lander mounting concept.
- Bolt preload conditions were revised to avoid artificial stress concentration in static simulations while maintaining joint integrity.

The updated structure design is shown in Figure 33(a). Additionally, in order for spacecraft to survive shock loads, reinforcement mounting structures were designed and integrated with the CubeSat-Based rover as shown in Figure 33(b).

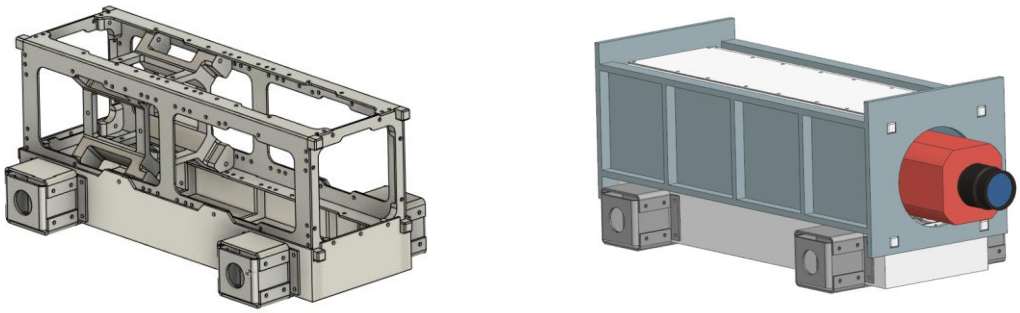

(a) Updated Internal Structure

(b) Updated Structure with Lunar Lander Mounting Structure

Figure 33: Updated Structure Design CAD Model

Following these design changes, all simulations were re-run and confirmed improved structural performance and compliance with all defined mission and launch requirements.

4.6 Updated FE Model

With the mounting structure added, the updated FE model is constrained at the mounting structure instead of the rover wheel as shown in orange in Figure 34.

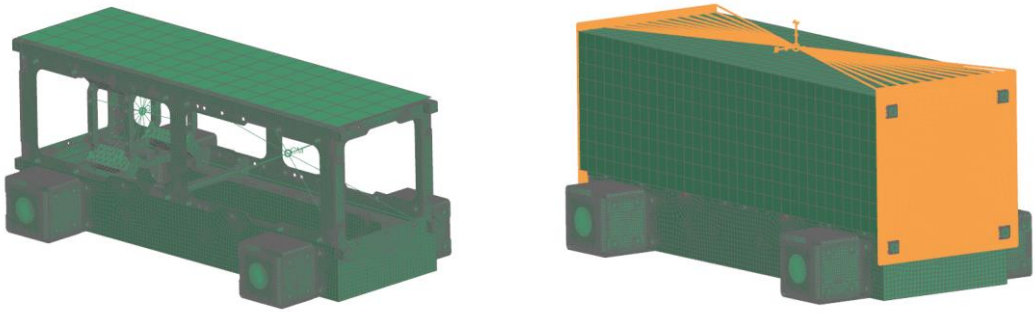

(a) Simplified model for FE analysis (b) Boundary conditions Highlighted

Figure 34: Updated FE model: (a) Simplified geometry without panel, (b) Applied boundary conditions in orange.

4.7 Updated Structural Design Simulation Results

While all analysis types were conducted again with the updated model, only modal analysis and SRS analysis results will be shown in order to maintain conciseness. Quasi-static and random vibration results show a more conservative results, while SRS analysis failed to meet the structural requirement in the previous design. Modal analysis will be shown as natural frequency shift was introduced due to the additional Lunar Lander mounting structure.

4.7.1 Modal Analysis Updated Results

The first two natural frequency modes of the updated FE model are 266.6 Hz and 342.0 Hz, respectively, as shown in Figure 35. While the first mode natural frequency is lower due to the introduction of lander mount, the updated model still exceeds the first mode natural frequency requirement of 115 Hz.

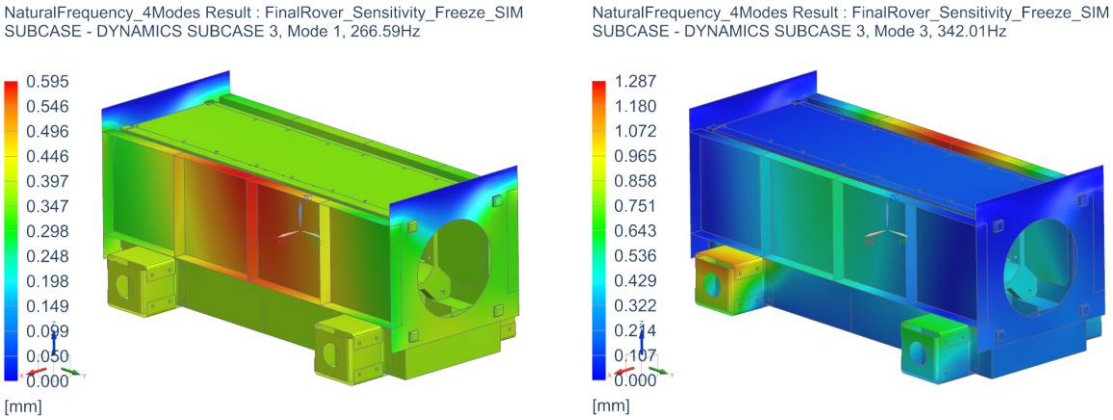

(a) First Natural Frequency: 266.6 Hz (b) Second Natural Frequency: 342.0 Hz

Figure 35: Updated Modal Analysis results: First and second mode natural frequencies

4.7.2 Shock Response Spectrum Analysis Updated Result

After the design change, the most severe load case for SRS analysis is still the Z-axis shock from Penegrine Lander Shock profile. The peak von Mises stress contour of the updated case is shown in Figure 36.

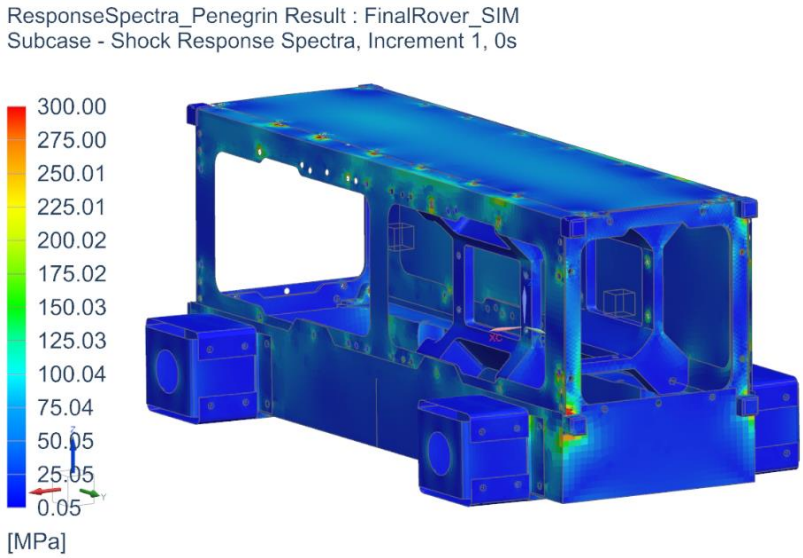

Figure 36: Shock Response Spectrum Analysis peak von Mises Stress contour.

The peak von Mises stress observed from the updated SRS analysis was **300 MPa**, which occurred at the Rover Chassis part. This yields a minimum margin of safety (MoS) of **0.10** under this worst-case loading condition, passing the structural requirement.

4.7.3 Model Sensitivity Analysis

After the design is finalized to have passed structural requirements, model sensitivity analysis was performed to determine the importance of each FE model input parameters. To perform sensitivity analysis, seven important input parameters, shown in Table 8, of the FE model will be varied. The variation range of each input parameters are summarized in Table 8 below:

Table 8: FE model Input Variable Summary for sensitivity analysis

Variable	Baseline Value	Range	Change in % from baseline
Aluminium Modulus (GPa)	70	63 – 77	±10%
Steel Modulus (GPa)	200	180 – 220	±10%
Total Mass (kg)	1.75	1.575 –1.925	±10%
Aluminium Part Thickness (mm)	2.0	1.8 – 2.2	±10%
Critical Damping Coefficient	5%	4.5% - 5.5%	±10%
Aluminium Poisson's Ratio	0.33	0.29 – 0.35	±10%
Steel Poisson's Ratio	0.28	0.252 – 0.308	±10%

All parameters range variation is put to 10% from the baseline to give equal weight to all variables for sensitivity analysis. 100 samples will be generated from this design space using Latin Hypercube sampling method.

With the updated FE model, Shock Response Spectrum Analysis and Modal analysis were simulated with 100 design samples. Displacement, maximum von Mises stress, and First mode natural frequency, were extracted from each design sample simulation result. The results are then postprocessed, using Ansys optiSLang, into uncertainty summary table shown in Table 9.

Table 9: EMEC2 Model Uncertainty Summary

Output Variable	**Baseline**	**Mean**	**Standard Deviation**	**CoV**
First mode frequency (Hz)	270.9	271.3	23.2 (8.6%)	0.086
Max Von Mises Stress SRS (MPa)	838.74	861.4	83.5 (10.0%)	0.097
Max Displacement SRS (mm)	2.48	2.50	0.27 (10.8%)	0.108

In sensitivity analysis using the Metamodel of Optimal Prognosis (MOP) method of Ansys optiSLang, insightful observations can be observed from Coefficient of Prognosis (CoP) matrix shown in Figure 37. Coefficient of Prognosis assesses the predictive quality of a metamodel and is also simultaneously used to evaluate the importance of input variables in sensitivity analysis.

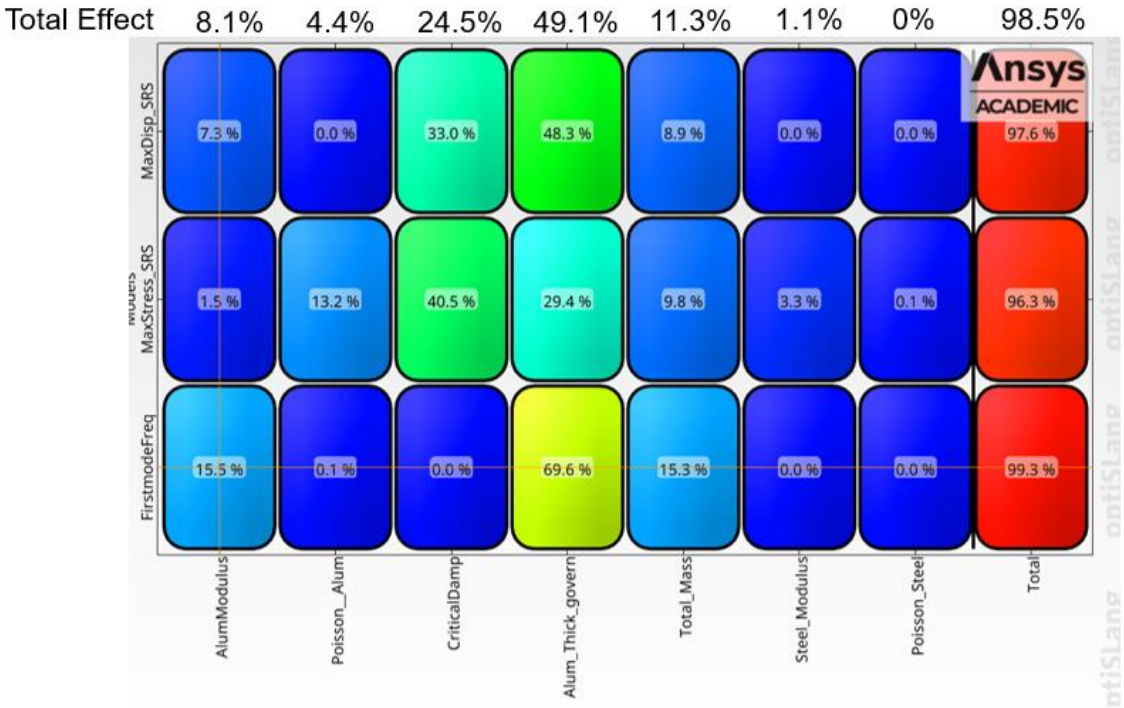

Figure 37: CoP Matrix of analysis results from 100 samples.

As the CoP matrix shows the relative influence of each input parameter to each response output sensitivity, in percentage, the following trends can be observed from Figure 37:

- Wall thickness is the most influential parameter having overall effect of 49% when all responses are averaged.
- Critical Damping has a significant effect of more than 30% on Stress and Displacement of shock analysis, but zero effect on first mode natural frequency.
- Total Mass and Aluminium Modulus have minor influences on all output responses.
- Steel Modulus and Poisson's ratios generally have less than 5% effect on output responses.

4.8 Model Validation Result

Using the optimization module mentioned in Section 3.5, the structural finite element model is optimized for minimal error between the natural frequency modes of synthetic data and the modal analysis result. The resulting modal analysis result is then compared with the synthetic data as shown in Table 10.

Table 10: Model Validation Result: Synthetic data vs Modal Analysis Result

Input Parameter	Synthetic Data Value	FEM Modal Analysis Value	Error (%)
Aluminium Modulus (GPa)	68.91	67.40	-2%
Aluminium Poisson's Ratio	0.324	0.316	-2.5%
Aluminium Thickness (mm)	1.84	1.90	3%
Total Mass (kg)	6.875	6.82	-1%
Steel Modulus (GPa)	220	217	-1%
Steel Poisson's Ratio	0.276	0.258	-7%
Response	Synthetic Data Result	FEM Modal Analysis Result	Error (%)
1st Mode Frequency (Hz)	268.87	273.90	2%
2nd Mode Frequency (Hz)	373.11	375.24	1%
3rd Mode Frequency (Hz)	434.48	429.00	-1%
4th Mode Frequency (Hz)	445.86	447.2	0.5%

This result shows the possible error that can occur when tuning the structural finite element model to represent a certain set of natural frequency modes data. If real-world experimental data shows similar natural frequency modes, the same order of error magnitude can be expected from FE model tuning.

4.9 System Requirement Verification

To conclude, the results have shown that the EMEC2 design met all major high level system requirements:

- Total Mass remains under 8 kg
- Volume of CubeSat component fits within allowable 3U CubeSat Standard dimensions
- Natural frequency of the CubeSat-based rover remains above 115 Hz
- Thermal range of internal components are between -40°C to +85°C (target operational envelope)
- Mobility performance validated for soft regolith analogue terrain

5 Discussion

The EMEC2 project contributes to the expanding field of CubeSat-based planetary rovers by demonstrating how standardized spacecraft platforms can be adapted for surface mobility while maintaining structural integrity and thermal viability. While previous efforts such as HiveR [11] and CubeRover [12] have advanced the concept of compact, mobile surface explorers, EMEC2 distinguishes itself by building upon a 3U CubeSat core platform, leveraging its modularity and existing deployment infrastructure. Although the rover exceeds the 3U form factor when deployed, the use of a 3U-based architecture streamlines development, integration, and potential rideshare compatibility.

This design philosophy reduces the engineering effort typically required for custom structures while enabling active planetary surface locomotion. Unlike CubeRover, which houses a CubeSat as a payload, EMEC2 integrates the CubeSat as part of the rover's structural frame. While conceptually similar to von Unwerth's work on HiveR, EMEC2 includes structurally validated mounting interfaces along with full-scale thermal and structural analysis which von Unwerth's work lacks.

Structurally, the system meets the critical launch environment criteria, achieving a first-mode natural frequency above 115 Hz and positive margins of safety under the worst-case shock response spectrum from commercial rideshare specifications. These results confirm that using 7075-T6 aluminium with 2.0 mm thickness as rover structure element is sufficient to maintain structural integrity of the CubeSat-Based Rover. It is also discovered that the additional mounting structure is necessary for EMEC2 to tolerate the most critical lunar landing shock load with 1.60 mm wall thickness for CubeSat structure parts which keep the structural weight minimum. EMEC2's adherence to the 3U CubeSat standard structure also simplifies integration with commercial off-the-shelf CubeSat subsystem components.

Through a passive thermal management system, the CubeSat-based rover can ensure thermal compliance throughout the mission. A combination of multilayer insulation (MLI) and tailored surface emissivity has been demonstrated to keep all onboard avionics within their operational temperature limits during the full 14-day lunar sunlit period.

Despite these strengths, additional validation is necessary. The damping characteristics of the structure, particularly the damping coefficient, require validation through real-world experimental data to ensure accurate dynamic response predictions. The high temperature change of PEEK wheels from +20℃ to +80℃ occurring daily between operating condition and idle condition can induce cyclic stress and loosening of mechanical parts. This should be further studied to ensure long-term mechanical integrity. Due to computational resource limitations, PEEK wheel is not included in FE model, and its thermal stress should be further studied. Moreover, while Earth-based sandy terrain testing provides valuable insights into the mobility capability of the CubeSat-based rover, it cannot fully replicate reduced gravity conditions or prolonged exposure to lunar regolith.

To assess the structural model sensitivity under parameter variation, Sensitivity analysis was performed using Latin Hypercube Sampling across a ±10% range for seven key input parameters. Results indicate that wall thickness is the dominant contributor to output variability, especially in natural frequency and SRS displacement responses. Critical

damping significantly affects stress and displacement predictions but has negligible influence on modal frequency. In contrast, parameters such as total mass and modulus have relatively minor effects, while Poisson's ratio contributes negligibly. These findings highlight which parameters should be prioritized in further physical testing and refinement, particularly for damping and geometric tolerance characterization.

The synthetic data-based model validation primarily serves to illustrate the level of error that can arise when tuning a structural finite element model to match a specific set of natural frequency modes. Rather than confirming the model's absolute accuracy, this process quantifies the expected deviation introduced by parameter fitting within plausible design variations. The resulting frequency errors—within approximately ±2%—indicate the inherent tuning margin when aligning the model with a reference dataset. If future experimental testing exhibits a similar distribution of mode shapes and frequencies, comparable levels of model-to-test discrepancy may be anticipated. Thus, this validation provides a practical benchmark for interpreting the reliability of future model calibration against real-world experimental data.

6 Conclusion

The EMEC2 study demonstrates that a standard 3U CubeSat platform can be effectively modified to support the integration, deployment, and operation of a structurally robust, thermally controlled, and mobility-capable lunar surface rover. Structural augmentations were implemented while preserving the core 3U CubeSat architecture, enabling the system to meet launcher and lunar lander load requirements—even with the addition of the rover system. The study also demonstrates that passive thermal control, including multilayer insulation and tailored surface properties, is sufficient to maintain subsystem temperatures within operational limits during lunar daytime missions. Furthermore, the use of the developed terramechanics analysis tools, validated through targeted field testing, proves effective for generating mobility predictions during the preliminary design phase. Together, these findings address the stated research question by showing that appropriate structural design and passive thermal strategies can enable reliable lunar landing and rover deployment from a CubeSat-class platform. EMEC2 thus offers a validated reference architecture that reduces the engineering burden and lowers the entry barrier for future lunar surface science missions using CubeSats. Ultimately, EMEC2 provides a partially validated and practical reference for future missions aiming to utilize CubeSat standardized platform for mobile lunar surface operations.

7 Future Recommendation

While the structural design and preliminary validation of the CubeSat-based lunar rover have demonstrated its feasibility for lunar surface deployment, several areas of development remain open for future development and improvement. The following recommendations are proposed to further mature the design and ensure mission readiness:

7.1 Radiation Tolerance Analysis

The current work has not yet addressed the effects of the lunar radiation environment on the CubeSat-based Rover onboard electronics. Future development should include analysis of total ionizing dose (TID) and single-event effects (SEE) on critical subsystems, such as the payload, OBC, EPS, and communication units. This is particularly important for 14-days exposure on the lunar surface, where radiation shielding strategies or fault-tolerant architectures may be required.

7.2 Dust Protection

Given the abrasive and adhesive nature of lunar regolith, future work should incorporate sealing and protection strategies to prevent dust infiltration into sensitive subsystems, such as rover motor, optics, and solar panels. This includes the development of sealed housings, gaskets, and potentially non-contact joint designs, especially around wheel hubs, bearings, and sensor enclosures.

7.3 Environmental Qualification Testing

Although the structural model has been validated through numerical simulation, full environmental qualification testing is still required. This includes thermal vacuum cycling, outgassing compliance verification, random vibration, and shock testing. The results from these tests should be used to validate and update the FE model to ensure a more accurate prediction of the structure response under various mission conditions. Lunar regolith simulants should also be used to perform mobility tests instead of beach sand to obtain a more accurate sinkage and traction performance.

7.4 Control Architecture for Rover Navigation

The current rover control architecture remains conceptual. It is recommended to develop an autonomous navigation system that utilizes onboard camera data for terrain classification, obstacle detection, and motion planning. Algorithms should be tailored for the available processing power of the selected EnduroSat OBC, and support return-to-lander behavior to enhance mission reliability.

7.5 Mechanical Deployment Design

The deployment mechanism of the rover is presently represented by a conceptual model. Detailed mechanical design includes cable lowering mechanism and mechanism for rover release at touchdown. Analysis should also be performed to evaluate deployment reliability, packaging constraints within the lander, and dynamic behavior during release. Prototyping and testing of the deployment sequence are essential for mission reliability.

7.6 Communication System Design

Although a mass allocation was made for the communication system, further design work is needed to finalize the antenna configuration and evaluate its performance. This includes link budget analysis, surface coverage modeling, and compatibility with lander, lunar relay, or direct-to-Earth communication architectures. The design must also consider mechanical integration and survivability in the lunar environment.

7.7 CubeSat-based Rover Standardization

The results of this research highlight the potential of CubeSat-based rovers as a viable and scalable platform for planetary surface exploration, but realizing this potential requires further efforts toward system-level standardization. While a working example mechanical interface design has been explored in this research, future developments should further define standard mechanical and electrical interfaces for compatibility between CubeSat buses and rover systems. For instance, from this research, the side panel in which the CubeSat component interfaces with the rover component can potentially be converted to an electrical interface point as the CubeSat component is no longer required to be sealed on the rover interface side. Further standardization work includes establishing standardized environmental qualification protocols—including dust ingress and wheel-soil interaction testing using regolith simulants—to ensure reliability while reducing redundant testing. In the long term, these efforts could culminate in a formal CubeSat Surface Mobility Standard, analogous to the CubeSat Design Specification for orbital missions, enabling interoperability, reducing development timelines, and shifting focus from integration challenges toward achieving more ambitious scientific and operational goals.

8 Bibliography

[1] Arianespace, „Ariane 6 User's Manual for Multi-Launch Service,” 2021. [Online]. Available: https://ariane.group/app/uploads/sites/4/2024/10/MLSs-users-manual-ed0.0.pdf. [Geopend 9 July 2025].

[2] Astrobotic Technology Inc., „Astrobotic Lunar Landers: Payload User’s Guide,” Astrobotic Technology Inc., August 2021. [Online]. Available: https://www.astrobotic.com/wp-content/uploads/2022/01/PUGLanders_011222.pdf. [Geopend 17 April 2025].

[3] G. Miron, J. Cave, A. Karim, B. Fortin, O. Toure, M. Lecourt en Y. F. Chen, „Analysis of Lunar Rover Radiators Heat Balance using Thermal Circuit Theory and Impact of Lunar Regolith on its Performance,” *International Journal of Scientific Research in Science and Technology,* vol. 10, pp. 324-331, 2023.

[4] M. Alhammadi, „Lunar Rover Wheels Design & Analysis,” Khalifa University, 2022.

[5] M. Raouf, Foing Bernard, F. F. Hesar, P. Ananwatanyoo, A. Rinon, U. Sonou, B. Cameron, E. Woest en P. R. Mitra, „Educational CubeSats: Remote Sensing of Earth and Lunar Surface,” in *European Lunar Symposium*, Munster, 2025.

[6] J. Puig-Suari, „Development of the Standard CubeSat Deployer and a CubeSat Class PicoSatellite,” *IEEE,* 2001.

[7] A. Lovascio, A. D. Orazio en V. Centonze, „Characterization of a COTS-Based RF Receiver for Cubesat Applications,” *Sensors,* 2020.

[8] JAXA, „EQUULEUS (EQUilibriUm Lunar-Earth point 6U Spacecraft) and OMOTENASHI,” 2018. [Online]. Available: https://www.eoportal.org/satellite-missions/equuleus. [Geopend 2025].

[9] A. Johnstone, „CubeSat Design Specification REV 14.1,” Cal Poly – San Luis Obispo, CA, 2022.

[10] C. a. o. Hardgrove, „LunaH-Map: A CubeSat to Map Hydrogen within the Permanently Shadowed Regions of the Moon’s South Pole,” in *Proceedings of the IEEE Aerospace Conference*, Big Sky Montana, 2021.

[11] M. v. Unwerth, L. Fox, M. Manthey, R. Mahoney, I. Kolek, I. Selvanathan, S. Stapperfend en E. Stoll, „Application of CubeSat Technologies for Research and Exploration on the Lunar Surface,” *Advances in Astronautics Science and Technology,* vol. 6, pp. 57-72, 2023.

[12] T. Oikawa, A. Almujahed, R. Rolley, T. Whitaker, C. C. D. La Fuente, T. Arbuckle, K. Quinn, A. Davis, C. Rampolla, J. Spoto, G. Purnell, J. Landrenaeu en M. Provenzano, „Plan and Progression of the Technology Readiness Level of the

CubeRover," in *Proceedings of the 74th International Astronautical Congress (IAC)*, Baku, Azerbaijan, 2023.

[13] M. v. Unwerth, L. Fox, M. Manthey, R. Mahoney, S. Stapperfend, I. Kolek, E. Stoll en I. Selvanathan, „Application of CubeSat Technologies for Research and Exploration," *Advances in Astronautics Science and Technology,* pp. 57-72, 2023.

[14] European Cooperation for Space Standardization, „ECSS-Q-ST-60-15C: Radiation hardness assurance - EEE components," 2012. [Online]. Available: https://ecss.nl/wp-content/uploads/standards/ecss-q/ECSS-Q-ST-60-15C1October2012.pdf. [Geopend 2025].

[15] L. Thomsen, T. M. Jordan en W. Girard, „Shielding Considerations for CubeSat Structures During Solar Maximum," in *37th Annual Small Satellite Conference*, 2023.

[16] EnduroSat, „Satellite Excellence Through Meticulous Qualification," EnduroSat, 2025. [Online]. Available: https://www.endurosat.com/space-qualification/. [Geopend 30 July 2025].

[17] A. Oe, S.-I. Nishida en S. Nakatani, „Study of passive steering mechanism for small Mars surface exploration rovers," *Journal of Terramechanics,* pp. 35-43, 2024.

[18] M. Sutoh, T. Hoshino en S. Wakabaya, „Rover deployment system for lunar landing mission," *Acta Astronautica,* pp. 454-461, 2017.

[19] P. McGarey, I. A. Nesnas, A. Rajguru, M. BezKrovny, V. Jamnejad, E. Sunada en L. Teitelbaum, „How to Deploy a 10-km Interferometric Radio Telescope on the Moon with Just Four Tethered Robots," in *IEEE Aerospace Conference*, 2022.

[20] Y.-k. Park, G.-N. Kim en S.-Y. Park, „Novel Structure and Thermal Design and Analysis for CubeSats in Formation Flying," *Aerospace,* 2021.

[21] C. Hays, D. Posada en A. Malik, „Structural Design and Impact Analysis of a 1.5U CubeSat on the Lunar Surface," Cornell University, 2022.

[22] M. K. Vakilzadeh, V. Yaghoubi, A. T. Johansson en T. J. Abrahamsson, „Stochastic finite element model calibration based on frequency responses and bootstrap sampling," *Mechanical Systems and Signal Processing,* pp. 180-198, 2017.

[23] J. J. Wijker, Spacecraft Structures, Leiden: Springer, 2008.

[24] European Cooperation for Space Standardization, „ECSS-E-HB-32-25A: Mechanical shock design and verification handbook," 14 July 2015. [Online]. Available: https://ecss.nl/wp-content/uploads/2015/07/ECSS-E-HB-32-25A(14July2015).pdf. [Geopend 2025].

[25] European Cooperation for Space Standardization, „ECSS-E-HB-32-26A: Spacecraft mechanical loads analysis handbook," 19 February 2013. [Online]. Available: https://ecss.nl/wp-content/uploads/handbooks/ecss-e-hb/ECSS-E-HB-32-26A19February2013.pdf. [Geopend 11 July 2025].

[26] T. Most en J. Will , „Sensitivity analysis using the Metamodel of Optimal Prognosis," DYNARDO– Dynamic Software and Engineering GmbH, Weimar, Germany, 2011.

[27] maxon, „ECX FLAT 22 L, Ø22 mm, brushless, with Hall sensors,” maxon, [Online]. Available: https://www.maxongroup.com/maxon/view/product/motor/ecmotor/ecflat/ECXflat22/ECXA22LZF50E6ILACO1Y546A. [Geopend 7 July 2025].

[28] maxon, „Planetary gearhead GPX 22 Ø22 mm, 3-stage,” maxon, [Online]. Available: https://www.maxongroup.com/maxon/view/product/gear/planetary/GPX/GPX22/GPX22-3-Stufig-A/GPX22AAKLSL0111CPLW. [Geopend 7 July 2025].

[29] maxon, „DEC Module 24/2,” maxon, [Online]. Available: https://www.maxongroup.com/maxon/view/product/control/1-Q-EC-Verstaerker/367661. [Geopend 7 July 2025].

[30] L. MatWeb, „Aluminum 7075-T6; 7075-T651 Material Data Sheet,” 2025. [Online]. Available: https://asm.matweb.com/search/specificmaterial.asp?bassnum=ma7075t6. [Geopend 17 April 2025].

[31] L. Matweb, „Overview of Materials for Polyetheretherketone, Unreinforced,” 2025. [Online]. Available: https://www.matweb.com/search/datasheet_print.aspx?matguid=2164cacabcde4391a596640d553b2ebe. [Geopend 17 April 2025].

[32] P. R. Mitra, „Structural Design and Analysis of an Earth Observation 3U,” Delft University of Technology, Delft, 2025.

[33] I. W. David Carrier, „Geotechnical Properties of Lunar Soil,” Lunar Geotechnical Institute, Lakeland, Florida, 2005.

[34] D. G. Gilmore, Spacecraft Thermal Control Handbook: Volume I, Fundamental Technologies, El Segundo, California and Reston, Virginia: The Aerospace Press and AIAA, 2002.

[35] I. Subedi, T. J. Silverman, M. G. Deceglie en N. J. Podraza, „Emissivity of solar cell cover glass calculated from infrared reflectance measurements,” *Solar Energy Materials and Solar Cells,* vol. 190, pp. 98-102, 2019.

[36] NASA, „Solar Absorptance and Thermal Emittance of Some Common Spacecraft Thermal-Control Coatings,” NASA reference publication, Greenbelt, Maryland, 1984.

[37] A. Riverola, A. Mellor, D. A. Alvarez, L. Ferre Llin, I. Guarracino, C. N. Markides, D. J. Paul, D. Chemisana en E. Daukes, „Mid-infrared emissivity of crystalline silicon solar cells,” *Solar Energy Materials and Solar Cells,* vol. 174, pp. 607 - 615, 2018.

[38] P. B. Hager, A. P. Tighe en F. W. Cipriani, „Theoretical Approach to Quantify Effects of Lunar Dust Deposition on Radiator Performance for Moon Exploration Missions,” in *52nd International Conference on Environmental Systems*, Calgary, Canada, 2023.

[39] A. R. Pacheco, „Solar Panel Array for 3U CubeSat to the Moon,” in *European Lunar Symposium 2025*, Münster, 2025.

[40] H. Wang, T. Zhang, S. Wang en S. To, „Characterization of the Friction Coefficient of Aluminum Alloy 6061 in Ultra-Precision Machining," *Metals,* vol. 10, p. 336, 2020.

[41] L. Matweb, „Aluminum 6082-T6 Material Data Sheet," 2025. [Online]. Available: https://www.matweb.com/search/datasheet.aspx?matguid=fad29be6e64d4e95a241690f1f6e1eb7&n=1&ckck=1. [Geopend 17 April 2025].

[42] A. Steels, „Stainless Steel 304: Properties, Composition & Applications," Atlas Steels, 2025. [Online]. Available: https://studylib.net/doc/25928004/aisi-340-info. [Geopend 17 April 2025].

[43] European Cooperation for Space Standardization, „ECSS-E-ST-32-10C: Structural factors of safety for spaceflight hardware," 2019. [Online]. Available: https://ecss.nl/wp-content/uploads/2019/09/ECSS-E-ST-32-10C_Rev.2-Corr.1(1August2019).pdf. [Geopend 2025].

[44] M. B. V. Guedes, „CubeSat Structural and Thermal Analysis Methodology ISTSat-1 Design," Instituto Superior Técnico, 2019.

[45] SpaceX, „Rideshare Payload User's Guide Version 10," 2024. [Online]. Available: https://storage.googleapis.com/rideshare-static/Rideshare_Payload_Users_Guide.pdf. [Geopend 9 July 2025].

[46] R. Lab, „Electron Payload User's Guide Version 7.0," 2022. [Online]. Available: https://rocketlabcorp.com/assets/Electron-Payload-User-Guide-7.0-v6.pdf. [Geopend 9 July 2025].

[47] Arianespace, „SSMS Vega-C User's Manual," 2020. [Online]. Available: https://ariane.group/app/uploads/sites/4/2024/10/SSMS-Vega-C-UsersManual-Issue-1-Rev0-Sept2020.pdf. [Geopend 9 July 2025].

[48] European Cooperation For Space Standardization, „ECSS-E-ST-31C: Thermal control general requirements," 15 November 2008. [Online]. Available: https://ecss.nl/wp-content/uploads/standards/ecss-e/ECSS-E-ST-31C15November2008.pdf. [Geopend 14 August 2025].

[49] J. M. G. S. D. V. B. T. Sonja Kostic, S. Kostic, J. Miljojkovic, G. Simunovic, D. Vukelic en B. Tadic, „Uncertainty in the determination of elastic modulus by tensile testing," *Engineering Science and Technology, an International Journal,* vol. 25, nr. 2215-0986, p. 100998, 2022.

[50] D. P. Malawey, „Mechanical Design and Optimization of a Standardized CubeSat," Texas A&M University, 2016.

[51] European Cooperation for Space Standardization, „ECSS-E-ST-10C Rev.1 – System engineering general requirements," 15 February 2017. [Online]. Available: https://ecss.nl/standard/ecss-e-st-10c-rev-1-system-engineering-general-requirements-15-february-2017/. [Geopend 30 July 2025].

[52] HYSPIM, „Hyperspectral camera," HYSPIM, [Online]. Available: https://www.hyspim.com/. [Geopend March 2025].

[53] EnduroSat, „S-Band Transceiver,” EnduroSat, [Online]. Available: https://www.endurosat.com/products/s-band-transceiver/. [Geopend 7 July 2025].

[54] EnduroSat, „S-BAND ANTENNA COMMERCIAL,” EnduroSat, [Online]. Available: https://www.endurosat.com/products/s-band-antenna-commercial/. [Geopend 7 July 2025].

[55] EnduroSat, „X-BAND TRANSMITTER,” EnduroSat, [Online]. Available: https://www.endurosat.com/products/x-band-transmitter/. [Geopend 7 July 2025].

[56] EnduroSat, „X-BAND PATCH ANTENNA,” EnduroSat, [Online]. Available: https://www.endurosat.com/products/x-band-patch-antenna/. [Geopend 7 July 2025].

[57] EnduroSat, „EPS II + BATTERY PACK,” EnduroSat, [Online]. Available: https://www.endurosat.com/products/eps-ii-battery-pack/. [Geopend 7 July 2025].

[58] EnduroSat, „3U Double Deployable Solar Array,” EnduroSat, [Online]. Available: https://www.endurosat.com/products/3u-double-deployable-solar-array-2/. [Geopend 7 July 2025].

[59] EnduroSat, „Onboard Computer with GNSS,” EnduroSat, [Online]. Available: https://www.endurosat.com/products/onboard-computer-with-gnss/. [Geopend 7 July 2025].

Appendix A: Wheel Sizing Code

The following Python script was developed to support the preliminary sizing and performance evaluation of a rover wheel designed for lunar surface operations. It implements a terramechanics-based analytical model to simulate wheel-soil interaction, incorporating Reece's and Wong's classical formulations according to Alhammadi methodology [15]. The model accounts for key physical parameters such as soil cohesion, internal friction, bulk density, and lunar gravity, as well as wheel geometry, slip ratio, and grouser effects. The code estimates key performance metrics including drawbar pull, normal force, torque, and sinkage as a function of slip ratio, using numerical integration and iterative methods to solve for contact pressures and stress distributions. The analysis is implemented in Python using NumPy, SciPy, and Matplotlib.

```
import numpy as np
import matplotlib.pyplot as plt
from scipy.integrate import simps, quad
from scipy.optimize import fsolve

# Soil and wheel parameters
r = 0.1  # Wheel radius (m)
b = 0.08  # Wheel width (m)
c = 1200  # Soil Cohesion coefficient
kc = 1350
kphi = 820000
kc_prime = 0.0  # Reece's modified cohesion coefficient
kphi_prime = 120.0  # Reece's friction coefficient
rho = 1540  # Soil bulk density (kg/m^3)
g = 1.62  # Lunar gravity (m/s^2)
n = 1.0  # Soil deformation exponent
a0 = 0.4    #max stress location constants
a1 = 0.25   #max stress location constants
kx = 0.012   #shear deformation modulus
phi_deg = 33.4   # Friction Angle in degree
phi = np.deg2rad(phi_deg)
W = 3.7      # nominal wheel load
grouser_number = 14

# c0 = c0_prime * grouser height + c1_prime
initial_grouser_height = 0.015 # m
lt = ((2*r + initial_grouser_height)/2) * np.sin(2*np.pi / grouser_number)
travel_dd = grouser_number * lt
ls = initial_grouser_height / np.tan((np.pi/4) - (phi/2))
r_prime = travel_dd / (2*np.pi)
c0_prime = 1.76  # dynamic sinkage constant
c1_prime = 0.012
c0 = c0_prime * initial_grouser_height + c1_prime # dynamic sinkage constant

if lt < ls:
    print(f"lt ({lt:.6f} m) < ls ({ls:.6f} m). Soil entrapment problem.")
else:
    print(f"lt ({lt:.6f} m) > ls ({ls:.6f} m). optimal traction.")

# Slip ratio and grouser height ranges
slip_ratio = np.linspace(0, 1, 200)  # Slip ratio from 0% to 100%
grouser_height = np.linspace(0, 0.08, 200)  # Grouser height from 0 to 5 cm

# Function to compute pressure at angle theta
def pressure(theta, kc_prime, kphi_prime, rho, g, r, l):
    """Calculate pressure at angle theta."""
    h = r * (np.cos(0) - np.cos(theta))  # Sinkage at given angle
```

```
    return (c * kc_prime + rho * g * l * kphi_prime) * (h / l) ** n

# Function to compute contact length
def contact_length(r, h_st, theta_st):
    """Compute wheel-soil contact length based on radius and sinkage."""
    return 2 * r * np.sin(theta_st)

# Function to solve for static sinkage & contact length iteratively
def compute_static_sinkage(vertical_force):
    """Iteratively solve for static sinkage and contact length."""
    h_st = 0.01  # Initial guess for sinkage
    tolerance = 1e-3  # Convergence tolerance
    max_iterations = 500  # Max iterations for convergence

    for iteration in range(max_iterations):
        theta_st = np.arccos(1 - (h_st / r))
        l = contact_length(r, h_st, theta_st)  # Compute contact length from
current sinkage
        #print(f"Current Static theta: {np.rad2deg(theta_st):.2f} degree")
        #print(f"Current Static Sinkage: {h_st * 1000:.2f} mm")

        # Integration function to solve for static sinkage
        theta = np.linspace(-theta_st, theta_st, 200)
        force_current = simps(pressure(theta, kc_prime, kphi_prime, rho, g, r,
l) * b * r * np.cos(theta), theta)
        #print(f"Current Weight: {force_current:.2f} N")

        # Check for convergence
        if abs(force_current - vertical_force) < tolerance:
            print(f"Converged in {iteration + 1} iterations!")
            break

        if force_current < vertical_force:
            h_st += 0.00005  # Increase sinkage if the current force is too low
        else:
            h_st -= 0.00005  # Decrease sinkage if the current force is too
high

        # Ensure h_st stays positive
        h_st = max(0.001, h_st)

    return h_st, l

# Compute Static Sinkage and Contact Length
h_static, l_static = compute_static_sinkage(W)
print(f"Static Sinkage: {h_static * 1000:.4f} mm")
print(f"Wheel Contact Length: {l_static:.4f} m")

# 1. Sinkage
def calculate_sinkage(c0, slip_ratio):
    """Calculate sinkage as a function of slip ratio."""
    h_total = h_static + (c0 * slip_ratio)  # Dynamic sinkage increases with
slip ratio
    return h_total

sinkage = calculate_sinkage(c0, slip_ratio)

#compaction resistance
# Discretize h for integration using simps
h = np.linspace(0, h_static, 200)

# Function for Rc integrand
def Rc_integrand(h, c, kc_prime, rho, g, l, kphi_prime, n):
    return (c * kc_prime + rho * g * l * kphi_prime) * (h / l) ** n

# Compute Rc using simps
Rc_values = Rc_integrand(h, c, kc_prime, rho, g, l_static, kphi_prime, n)
```

```
Rc = simps(Rc_values, h)
print(f"Resistance force (Rc): {Rc:.4f} N")

# 2. Force Calculation
def bulldozing_resistance(h, phi):
    epsilon = np.arccos(1 - (2 * h / r))
    k_c = (1 - np.tan(phi)) * np.cos(phi)**2
    k_rho = (2 / np.tan(phi) + 1) * np.cos(phi)**2
    l_r = h * np.tan(np.deg2rad(45 - phi / 2))**2
    term1 = (b * np.sin(epsilon + phi) * (2 * c * k_c * h + rho * g * k_rho *
h**2)) / (2 * np.sin(epsilon) * np.cos(phi))
    term2 = (np.pi * (90-phi) * rho * g * l_r**2) / 540
    term3 = ((np.pi * c * l_r**2)/180) + ((c * l_r**2) * np.tan(np.deg2rad(45 +
phi / 2)))
    R_b = term1 + term2 + term3
    return R_b
Rb_value = bulldozing_resistance(h_static, phi)
print(f"Resistance force (Rb): {Rb_value:.4f} N")

def compute_forces_for_slip(s, h_g):
    """
    1) Compute dynamic sinkage from slip.
    2) From that sinkage, define the front (entry) angle.
    3) Solve for sigma_max by matching W (vertical force).
    4) Integrate to get F_x, F_y, T.

    Returns F_x, F_y, T, sigma_max
    """

    h_total = h_static + c0 * s
    theta_entry = np.arccos((r - h_total) / (r+h_g))
    theta_m = (a0 + (a1 * s)) * theta_entry
    k_entryconst = 0.3
    theta_departure = -np.arccos((r - k_entryconst * h_static) / (r+h_g))
    alpha = theta_entry - theta_departure
    beta = 2*np.pi / grouser_number

    if np.isnan(theta_entry) or np.isnan(theta_departure):
        raise ValueError(f"Invalid theta values: theta_entry={theta_entry},
theta_departure={theta_departure}")

    def jx(theta):
        """
        Shear displacement for driving wheel, per Wong or Sutoh:
        jx = r * [ (theta_f - theta) - (1 - s)*(sin(theta_f) - sin(theta)) ]
        """
        return r * ((theta_entry - theta) - ((1.0 - s)*(np.sin(theta_entry) -
np.sin(theta))))

    # Function to compute normal stress at angle theta
    def sigma_of_theta(theta, sigma_max):
        """
        Piecewise normal stress distribution:
        - For theta <= theta_m:   (sigma_max/2) [cos( pi*(theta_m -
theta)/(theta_m - theta_r) ) + 1]
        - For theta >= theta_m:   (sigma_max/2) [cos( pi*(theta -
theta_m)/(theta_f - theta_m) ) + 1]
        """
        if theta <= theta_m:
            # Region from theta_r to theta_m
            return 0.5 * sigma_max * (np.cos(np.pi*(theta_m - theta)/(theta_m -
theta_departure)) + 1.0)
        else:
            # Region from theta_m to theta_f
            return 0.5 * sigma_max * (np.cos(np.pi*(theta -
theta_m)/(theta_entry - theta_m)) + 1.0)
```

```
    # Function to compute shear stress at angle theta
    def tau_x(theta, sigma_val):
        """
        tau_x(theta) = [ c + sigma_val*tan(phi) ] * [ 1 - exp( - jx(theta)/kx )
]
        """
        return ( c + sigma_val*np.tan(phi) ) * (1.0 - np.exp(- jx(theta)/kx))

    def fg(theta, h_g, sig_max):
        """
        Compute induced force per grouser based on the pressure model.
        """
        N_phi = np.tan(np.deg2rad(45-(phi_deg/2)) + phi) ** 2
        sigma_g = (0.5 * rho * g * h_g * N_phi) + (sig_max*N_phi) + (2 * c *
np.sqrt(N_phi))
        return b * sigma_g * h_g  # Force per unit length

    def compute_grouser_forces(s, r, h_g, theta_m, beta, sig_max):
        # Integrate for Fxg, Fyg, and Tg
        Fxg, _ = quad(lambda theta: fg(theta, h_g, sig_max) * np.cos(theta),
theta_m-(beta/2), theta_m+(beta/2))
        Fyg, _ = quad(lambda theta: fg(theta, h_g, sig_max) * np.sin(theta),
theta_m-(beta/2), theta_m+(beta/2))
        Tg, _ = quad(lambda theta: fg(theta, h_g, sig_max), theta_m-(beta/2),
theta_m+(beta/2))
        Fxg *= s * grouser_number / (2*np.pi)  # Apply moment arm
        Fyg *= s * grouser_number / (2*np.pi)  # Apply moment arm
        Tg *= (r + 0.6667 * h_g) * s * grouser_number / (2*np.pi)  # Apply
moment arm

        return Fxg, Fyg, Tg

    '''
    if alpha < beta:
        print(f"alpha < beta")
    else:
        Fxg, Fyg, Tg = compute_grouser_forces(r, h_g, theta_m, beta)
    '''
    #Vertical force from stress
    def vertical_force_residual(sigma_max_guess):
        # Discretize contact patch
        thetas = np.linspace(theta_departure, theta_entry, 100)
        Fxg, Fyg, Tg = compute_grouser_forces(s, r, h_g, theta_m, beta,
sigma_max_guess)
        # Build integrand
        integrand_vals = []
        for th in thetas:
            sig_th = float(sigma_of_theta(th, sigma_max_guess))
            tau_th = float(tau_x(th, sig_th))
            if np.isnan(sig_th) or np.isnan(tau_th):
                raise ValueError(f"NaN detected: theta={th:.4f},
sigma={sig_th:.4f}, tau={tau_th:.4f}")
            if np.isinf(sig_th) or np.isinf(tau_th):
                raise ValueError(f"Inf detected: theta={th:.4f},
sigma={sig_th:.4f}, tau={tau_th:.4f}")

            # vertical component from shear + normal
            integrand_vals.append(tau_th*np.sin(th) + sig_th*np.cos(th))

        # Numerically integrate (trapezoid rule)
        if len(integrand_vals) != len(thetas):
            raise ValueError(f"Dimension mismatch: integrand_vals has length
{len(integrand_vals)}, "
                             f"thetas has length {len(thetas)}")
        Fy = (r*b * np.trapz(integrand_vals, thetas)) + Fyg

        return Fy - W  # we want this to be zero
```

```
    #Solve for Sigma_max
    initial_guess = 2000.0  # [Pa], some initial guess
    sigma_max_solution = fsolve(vertical_force_residual, x0=initial_guess)[0]

    # print(f"Solved sigma_max = {sigma_max_solution:.3f} Pa")

    # ----------------------------------------
    # 7) Compute final forces: F_x, F_y, T
    # ----------------------------------------
    def compute_forces_torque(sigma_max_val):
        thetas = np.linspace(theta_departure, theta_entry, 100)

        # We will integrate for each quantity
        integrand_fx = []
        integrand_fy = []
        integrand_t  = []
        Fxg, Fyg, Tg = compute_grouser_forces(s, r, h_g, theta_m, beta,
sigma_max_val)

        for th in thetas:
            sig_th  = float(sigma_of_theta(th, sigma_max_val))
            tau_th  = float(tau_x(th, sig_th))
            # x-direction force (drawbar pull):
            integrand_fx.append(tau_th*np.cos(th) - sig_th*np.sin(th))

            # y-direction force:
            integrand_fy.append(tau_th*np.sin(th) + sig_th*np.cos(th))

            # torque about wheel center:
            # T = ∫(r * tau_x * r*b ) dtheta = r^2 * b * ∫ tau_x dtheta
            # We'll do it explicitly:
            integrand_t.append(tau_th)

        F_x = r*b * np.trapz(integrand_fx, thetas)
        F_y = r*b * np.trapz(integrand_fy, thetas)
        # multiply by b outside, times r in integrand => r*b for integrand,
plus another r => r^2 * b
        T   = r**2 * b * np.trapz(integrand_t, thetas)

        F_x_prime = F_x + Fxg
        F_y_prime = F_y + Fyg
        T_prime = T + Tg
        #eta = F_x_prime * (1-slip_ratio) * r_prime / T_prime

        return F_x_prime, F_y_prime, T_prime

    F_x, F_y, T = compute_forces_torque(sigma_max_solution)

    return F_x, F_y, T, sigma_max_solution

# Calculate values for plots
Fx_array = []
Fy_array = []
T_array  = []
sigma_max_array = []

h_g = initial_grouser_height

for s in slip_ratio:
    Fx, Fy, T, sigmamax = compute_forces_for_slip(s, h_g)
    Fx_array.append(Fx)
    Fy_array.append(Fy)
    T_array.append(T)
    sigma_max_array.append(sigmamax)

Fx_array = np.array(Fx_array)
```

```
Fy_array = np.array(Fy_array)
T_array  = np.array(T_array)
sigma_max_array = np.array(sigma_max_array)

# ================
# Plot results
# ================
plt.figure(figsize=(9,5))
plt.plot(slip_ratio, Fx_array, 'r-o', label='Drawbar Pull (Fx) [N]')
plt.plot(slip_ratio, Fy_array, 'b--', label='Vertical Force (Fy) [N]')
plt.plot(slip_ratio, T_array,  'g-.', label='Torque [N m]')
plt.xlabel('Slip Ratio [-]')
plt.ylabel('Value')
plt.legend()
plt.title('Wheel Forces vs Slip Ratio')
plt.grid(True)
plt.show()

# Plot 1: Sinkage vs Slip Ratio
plt.figure(figsize=(10, 6))
plt.plot(slip_ratio * 100, sinkage * 1000, label="Sinkage")
plt.xlabel("Slip Ratio (%)")
plt.ylabel("Sinkage (mm)")
plt.title("Sinkage vs Slip Ratio")
plt.grid(True)
plt.legend()
plt.show()
```

Appendix B: Rover Control Code

The following code was developed using Arduino IDE version 2.3.4 and is intended for execution on an Arduino UNO R3 microcontroller. It implements a basic four-wheel differential drive system using joystick inputs and pulse-width modulation (PWM) signals. The motor control is achieved through an L298H dual H-bridge motor driver module, enabling bidirectional control of four DC motors corresponding to the rover's left-front, left-rear, right-front, and right-rear wheels. This setup supports both forward/reverse movement and turning maneuvers based on analog joystick input, which can be changed to remotely commanded through serial communication. The code was used for initial mobility testing and verification of motor functionality in the prototype CubeSat-based rover.

```
int PWM1 = 9; // Motor 1 Rear Right
int IN1 = 4;
int IN2 = 5;
int PWM2 = 3; // Motor 2 Rear Left
int IN3 = 6;
int IN4 = 7;

int PWM3 = 10;  // Motor 3 (Front Right)
int IN5 = 8;
int IN6 = 2;

int PWM4 = 11;   // Motor 4 (Front Left)
int IN7 = 12;
int IN8 = 13;

int motorSpeedLeft = 0;
int motorSpeedRight = 0;

void setup() {
  Serial.begin(9600);

  // Set all motor pins as output
  pinMode(PWM1, OUTPUT); pinMode(IN1, OUTPUT); pinMode(IN2, OUTPUT);
  pinMode(PWM2, OUTPUT); pinMode(IN3, OUTPUT); pinMode(IN4, OUTPUT);
  pinMode(PWM3, OUTPUT); pinMode(IN5, OUTPUT); pinMode(IN6, OUTPUT);
  pinMode(PWM4, OUTPUT); pinMode(IN7, OUTPUT); pinMode(IN8, OUTPUT);
}

void loop() {
  int xAxis = analogRead(A0); // Left/Right
  int yAxis = analogRead(A1); // Forward/Backward

  //Serial.print("xAxis: ");
  //Serial.print(xAxis);
  //Serial.print(" | yAxis: ");
  //Serial.println(yAxis);

  // Y-axis: forward/backward motion
  if (yAxis < 470) {
    // Reverse
    digitalWrite(IN1, HIGH); digitalWrite(IN2, LOW); // RR
    digitalWrite(IN3, HIGH); digitalWrite(IN4, LOW); // RL
    digitalWrite(IN5, HIGH); digitalWrite(IN6, LOW); // FR
    digitalWrite(IN7, HIGH); digitalWrite(IN8, LOW); // FL

    motorSpeedRight = map(yAxis, 470, 0, 0, 255);
    motorSpeedLeft = map(yAxis, 470, 0, 0, 255);
```

```
  }
  else if (yAxis > 550) {
    // Forward
    digitalWrite(IN1, LOW); digitalWrite(IN2, HIGH); // RR
    digitalWrite(IN3, LOW); digitalWrite(IN4, HIGH); // RL
    digitalWrite(IN5, LOW); digitalWrite(IN6, HIGH); // FR
    digitalWrite(IN7, LOW); digitalWrite(IN8, HIGH); // FL

    motorSpeedRight = map(yAxis, 550, 1023, 0, 255);
    motorSpeedLeft = map(yAxis, 550, 1023, 0, 255);
  }
  else {
    motorSpeedRight = 0;
    motorSpeedLeft = 0;
  }

  // X-axis: turning
  if (xAxis < 470) {
    int xMapped = map(xAxis, 470, 0, 0, 255);
    motorSpeedLeft = motorSpeedLeft - xMapped;
    motorSpeedRight = motorSpeedRight + xMapped;

    if (motorSpeedLeft < 0) motorSpeedLeft = 0;
    if (motorSpeedRight > 255) motorSpeedRight = 255;
  }
  else if (xAxis > 550) {
    int xMapped = map(xAxis, 550, 1023, 0, 255);
    motorSpeedLeft = motorSpeedLeft + xMapped;
    motorSpeedRight = motorSpeedRight - xMapped;

    if (motorSpeedLeft > 255) motorSpeedLeft = 255;
    if (motorSpeedRight < 0) motorSpeedRight = 0;
  }

  // Prevent low PWM buzzing
  if (motorSpeedLeft < 50) motorSpeedLeft = 0;
  if (motorSpeedRight < 50) motorSpeedRight = 0;

  // Apply speed to motors
  analogWrite(PWM1, motorSpeedRight); // Rear Right
  analogWrite(PWM3, motorSpeedRight); // Front Right
  analogWrite(PWM2, motorSpeedLeft);  // Rear Left
  analogWrite(PWM4, motorSpeedLeft);  // Front Left
}
```

Appendix C: Structural Analysis Results

This appendix presents the structural analysis results for all non-critical load cases considered during the mechanical verification of the CubeSat-based rover. While these cases did not govern the final design—based on maximum stress, displacement, or safety margin, they were nonetheless evaluated to ensure comprehensive coverage of all mission-relevant loading scenarios. The results include stress distributions, deformation plots, and safety margin evaluations for various quasi-static, vibrational, and shock inputs corresponding to secondary launch and landing conditions. These analyses confirm that the structural integrity of the system is maintained across all expected operational environments, even in non-critical load scenarios, thereby supporting the overall robustness and reliability of the design.

- Quasi static Analysis

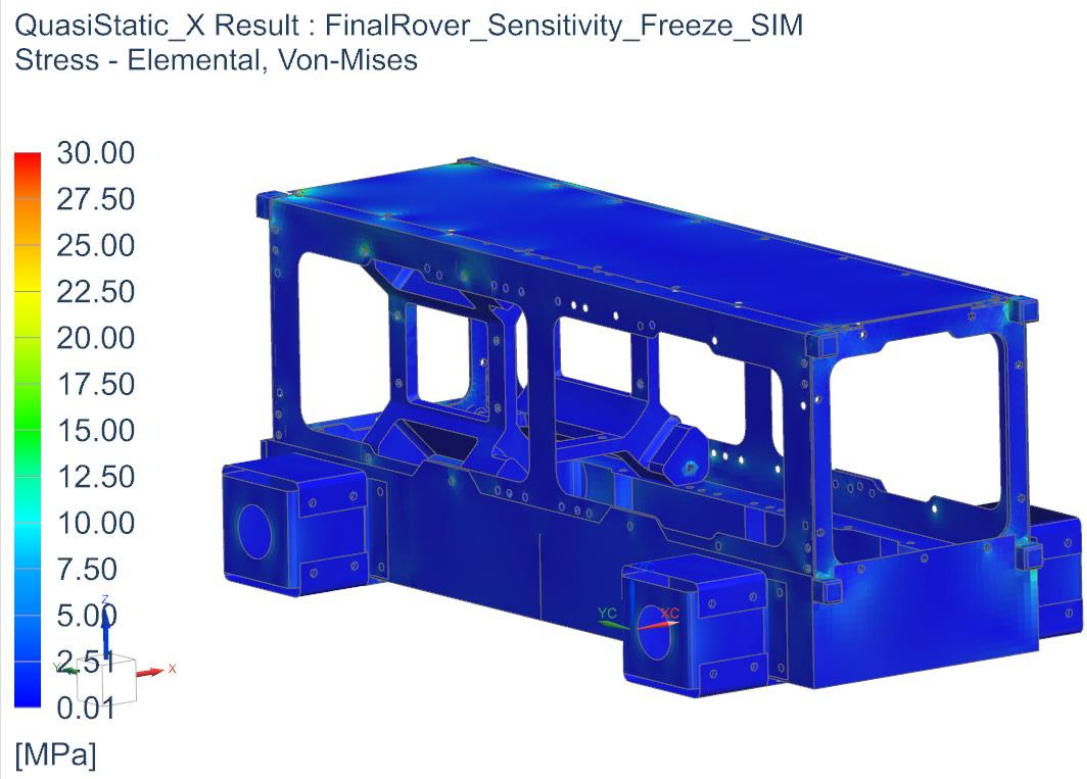

Figure 38: Quasi-Static Updated Design +17g X-axis Acceleration: Von mises Stress

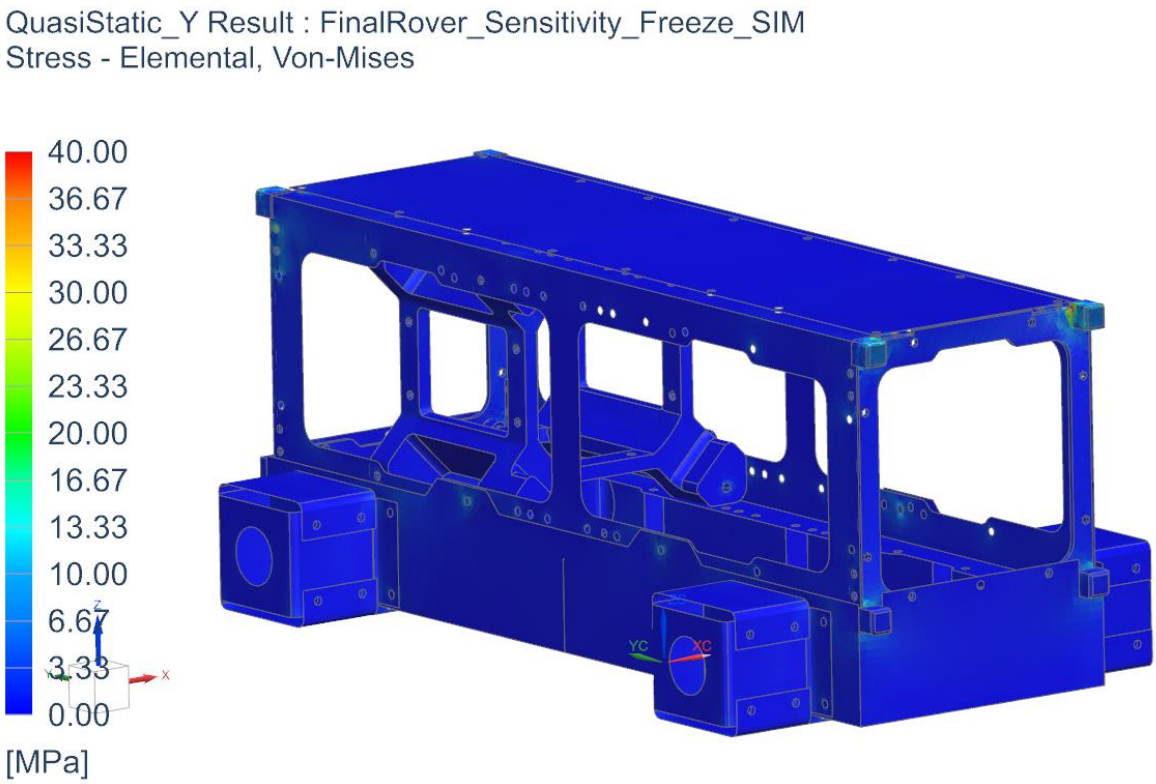

Figure 39: Quasi-Static Updated Design +17g Y-axis Acceleration: Von mises Stress

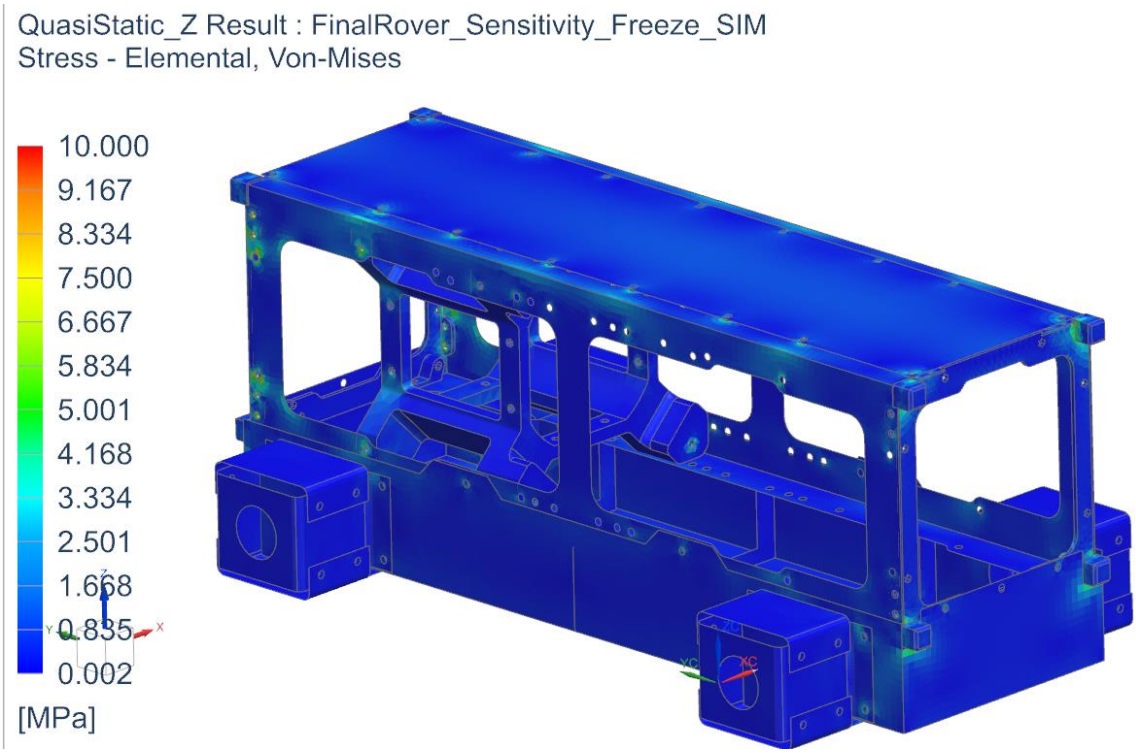

Figure 40: Quasi-Static Updated Design +10g Z-axis Acceleration: Von mises Stress

- Random Vibration Analysis

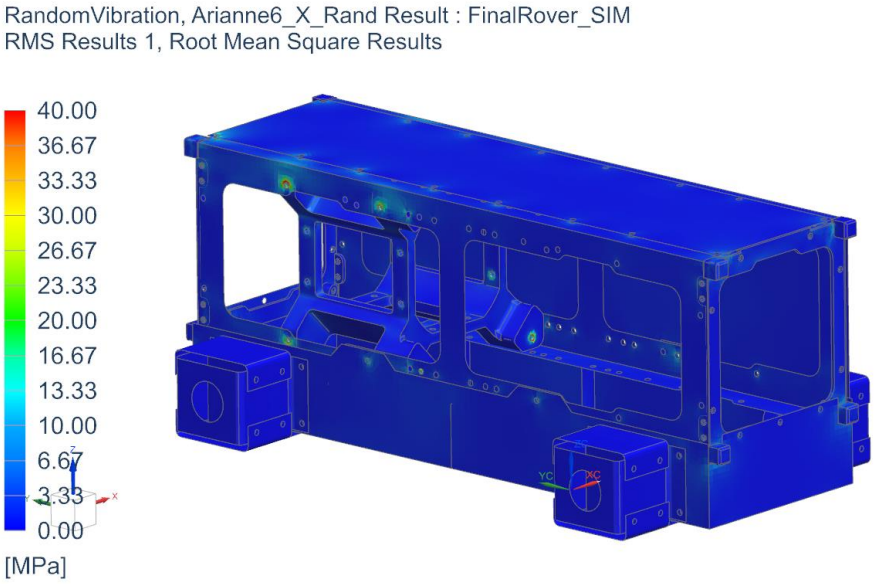

Figure 41: Updated Design Arianne 6 X-axis Random Vibration: RMS Von mises Stress

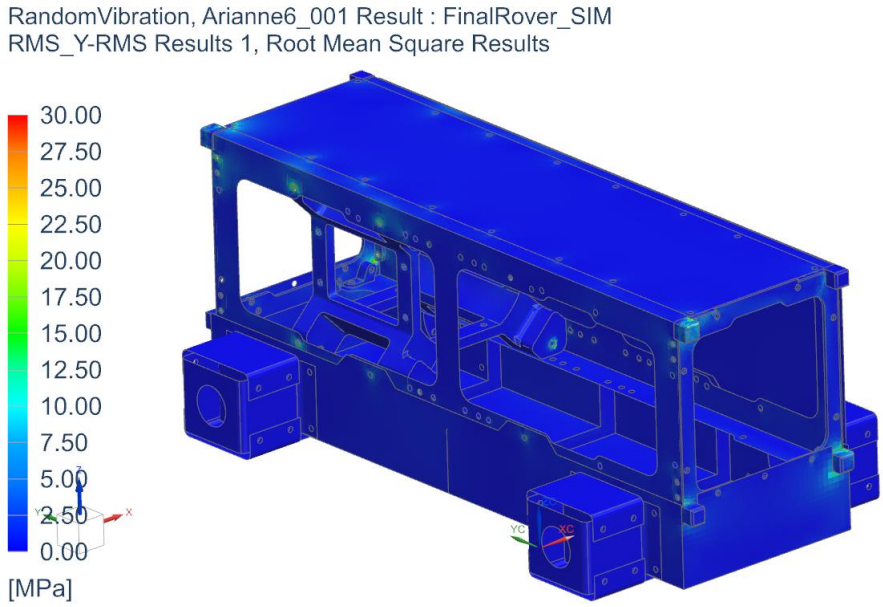

Figure 42: Updated Design Arianne 6 Y-axis Random Vibration: RMS Von mises Stress

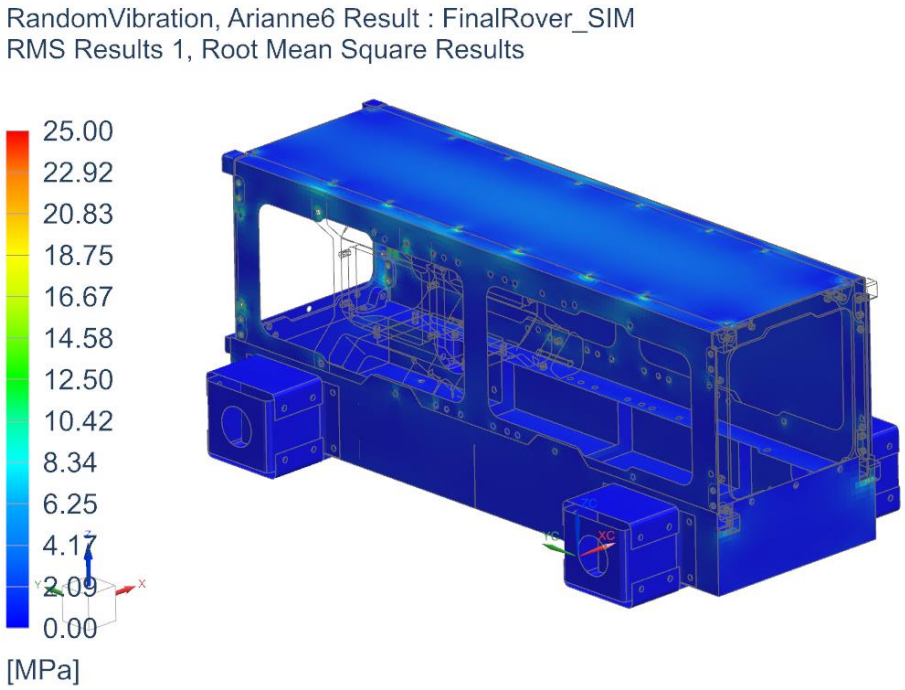

Figure 43: Updated Design Arianne 6 Z-axis Random Vibration: RMS Von mises Stress

- Shock Response Spectrum Analysis

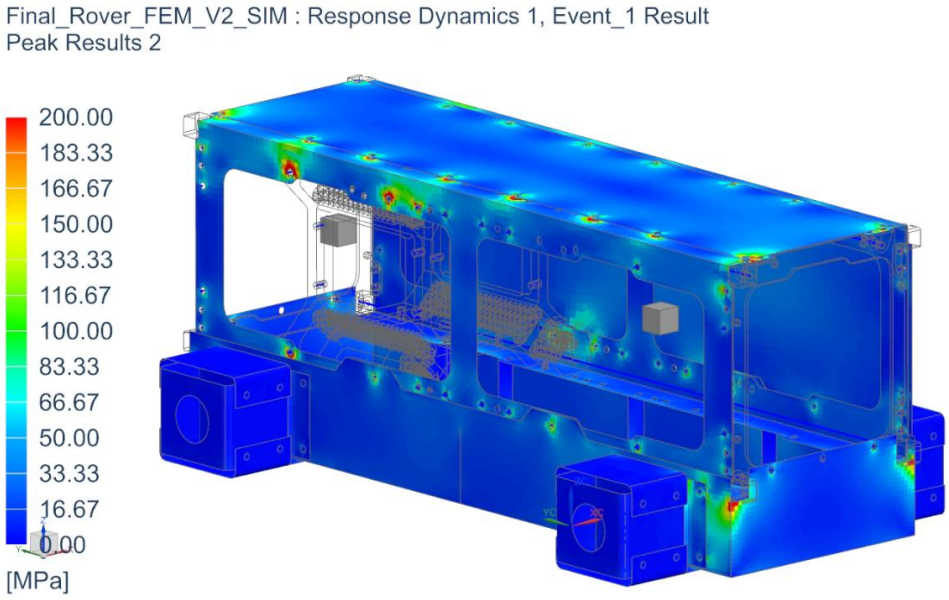

Figure 44: Updated Design Falcon 9 X-axis Shock: Peak Von mises Stress

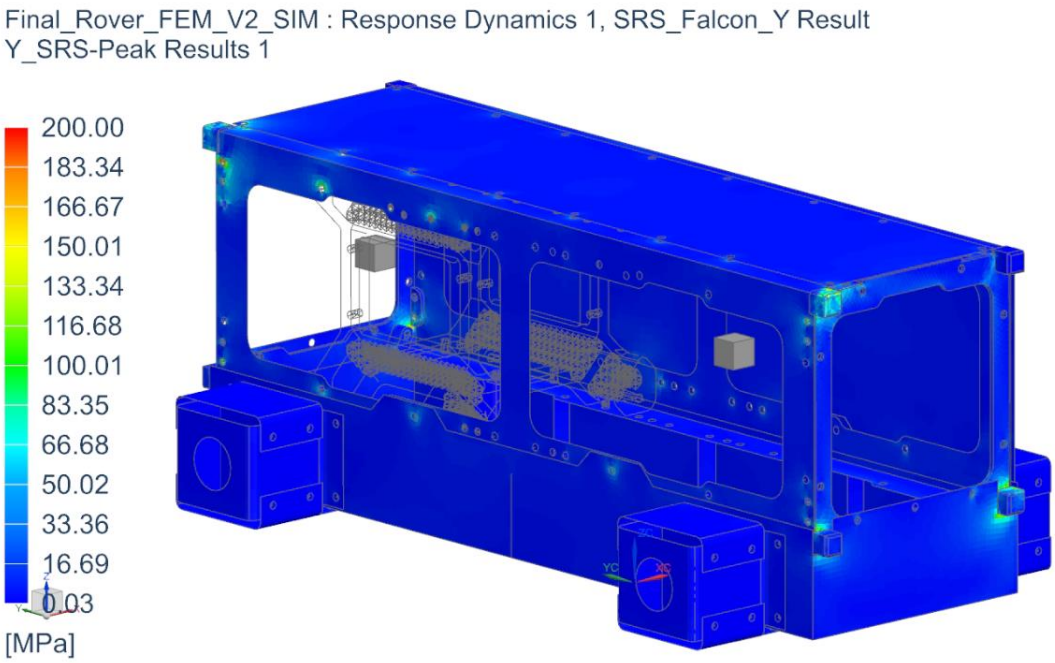

Figure 45: Updated Design Falcon 9 Y-axis Shock: Peak Von mises Stress

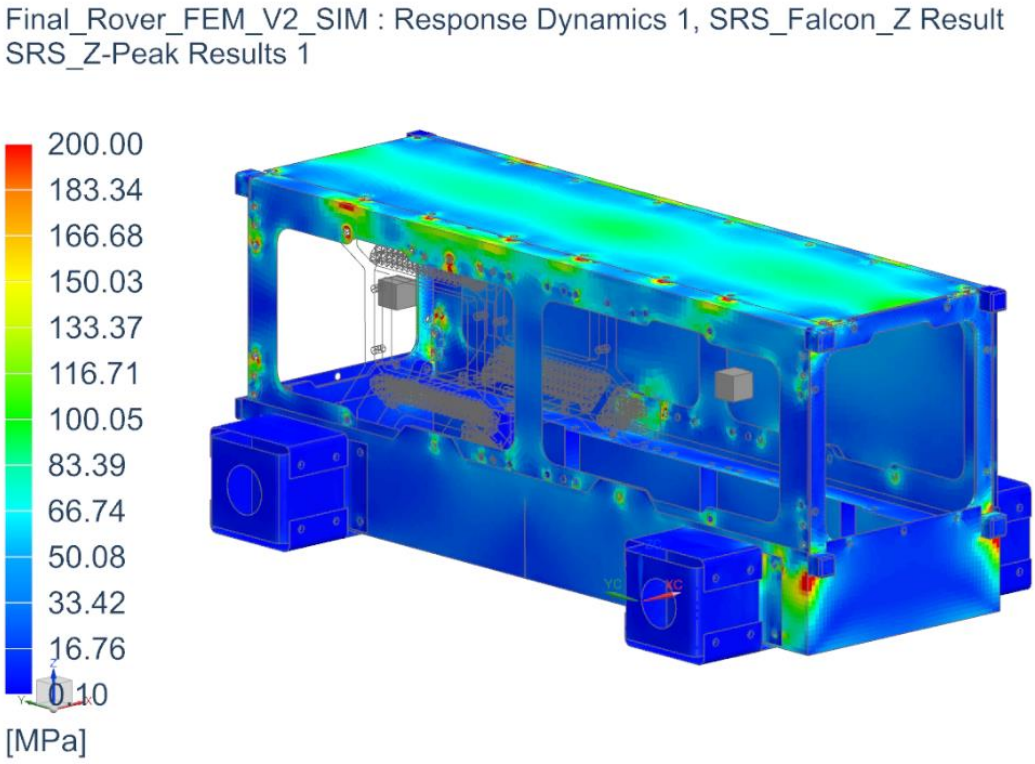

Figure 46: Updated Design Falcon 9 Z-axis Shock: Peak Von mises Stress

- Thermoelastic Analysis

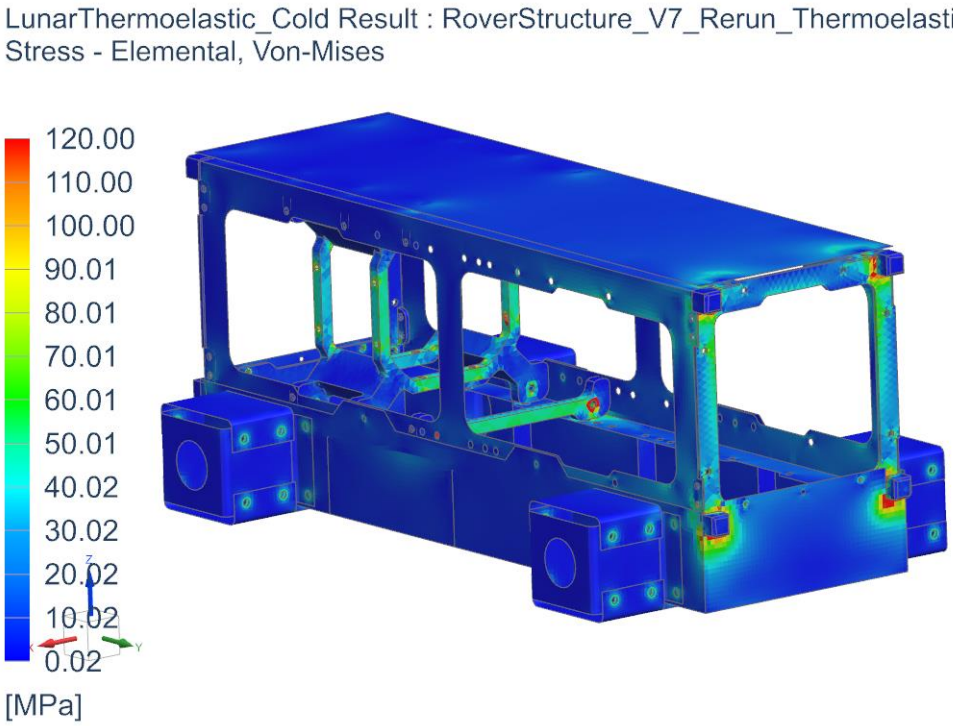

Figure 47: Initial Design Lunar Surface Idle Load (Cold) Thermoelastic Load Case: Von mises Stress